JGR Solid Earth

RESEARCH ARTICLE
10.1029/2023JB028011

Rock Anisotropy Promotes Hydraulic Fracture Containment at Depth

Guanyi Lu[1,2], Seyyedmaalek Momeni[1], Carlo Peruzzo[1], Fatima-Ezzahra Moukhtari[1,3], and Brice Lecampion[1]

[1]Geo-Energy Laboratory—Gaznat Chair, Institute of Civil Engineering, École Polytechnique Fédérale de Lausanne (EPFL), Lausanne, Switzerland, [2]Now at University of Pittsburgh, Pittsburgh, PA, USA, [3]Ingphi SA, Lausanne, Switzerland

Key Points:

- Intrinsic anisotropy of sedimentary rocks enhances the horizontal extension and hinders the vertical growth of hydraulic fractures
- The degree of fracture elongation depends on injection parameters and material properties through a dimensionless toughness coefficient
- Elongation is larger for toughness dominated compared to viscous dominated fractures

Supporting Information:

Supporting Information may be found in the online version of this article.

Correspondence to:

B. Lecampion,
brice.lecampion@epfl.ch

Citation:

Lu, G., Momeni, S., Peruzzo, C., Moukhtari, F.-E., & Lecampion, B. (2024). Rock anisotropy promotes hydraulic fracture containment at depth. *Journal of Geophysical Research: Solid Earth*, *129*, e2023JB028011. https://doi.org/10.1029/2023JB028011

Received 5 OCT 2023
Accepted 29 MAR 2024

Author Contributions:

Conceptualization: Guanyi Lu, Brice Lecampion
Data curation: Guanyi Lu, Seyyedmaalek Momeni, Carlo Peruzzo
Formal analysis: Guanyi Lu, Seyyedmaalek Momeni, Carlo Peruzzo, Fatima-Ezzahra Moukhtari, Brice Lecampion
Funding acquisition: Brice Lecampion
Investigation: Guanyi Lu, Seyyedmaalek Momeni, Carlo Peruzzo
Methodology: Guanyi Lu, Seyyedmaalek Momeni, Carlo Peruzzo, Brice Lecampion
Supervision: Brice Lecampion

Abstract We report laboratory experiments and numerical simulations demonstrating that the anisotropic characteristics of rocks play a major role in the elongation of hydraulic fractures (HFs) propagating in a plane perpendicular to the rocks' inherent layering (the bedding planes in sedimentary rocks and foliation planes in metamorphic rocks). Transverse anisotropy leads to larger HF extension in the parallel-to-layers/divider direction compared to the perpendicular-to-layers/arrester direction. This directly promotes vertical containment of HFs in most sedimentary basins worldwide even in the absence of any favorable in-situ stress contrasts or other material heterogeneities. More importantly, the ratio of the energy dissipated in fluid viscous flow in the fracture to the energy dissipated in the creation of new surfaces is found to play a critical role on fracture elongation, with fracture-energy dominated HFs being the most elongated while the viscous dominated ones remain more circular. These results open the door to a better engineering and control of HFs containment at depth in view of the competition between material anisotropy (both elastic stiffnesses and fracture toughness anisotropy) and injection parameters (fluid viscosity and rate of injection).

Plain Language Summary The widespread application of hydraulic fracturing for unconventional hydrocarbon production has prompted concerns about fractures extending vertically to sensitive rock layers, highlighting the need to understand fluid-driven fracturing for informed public discourse and improved industrial practices. Through numerical simulations and laboratory experiments on an analog transversely isotropic metamorphic rock, we show that the intrinsic anisotropic characteristics of sedimentary rocks lead to limited hydraulic fracture (HF) height growth across the bedding planes in the most common geological situations in unconventional reservoirs. Furthermore, we quantify the roles of elastic stiffnesses, fracture toughness, as well as the fluid injection conditions in shaping HF in transversely isotropic rocks. Our findings suggest that the HF is most elongated in the toughness-dominated regime, and the impact of rock anisotropy vanishes when the fracture propagates in the viscosity-dominated regime.

1. Introduction

Hydraulic fractures are widely used for the production enhancement of wells in unconventional hydro-carbon resources among other applications (Detournay, 2016). These tensile fractures propagate quasi-statically in rocks due to the injection of fluid at pressures greater than the minimum in-situ compressive stress. These fractures grow perpendicular to the minimum in-situ stress direction, which is in most sedimentary basins horizontal, such that hydraulic fractures (HFs) propagate vertically (Hubbert & Willis, 1957). Controlling the vertical height growth of a HF has long been considered a key factor for successful applications since the desire is to create a fracture that extends to the full height of the reservoir, while preventing excessive vertical growth that could create communication pathways for unwanted fluid migration into adjacent strata (Bunger & Lecampion, 2017; Economides & Nolte, 2000; Fisher & Warpinski, 2012). Over the years, concerns have been raised over serious environmental issues, such as contamination of underground drinking water resources by upward migration of fracturing fluid (EPA, 2016; Howarth & Ingraffea, 2011; Osborn et al., 2011; Vengosh et al., 2014; Vidic et al., 2013; Warner et al., 2012) and compromised seal integrity of the caprock in geologic carbon sequestration (Fu et al., 2017; Schrag, 2007), both of which may happen as a result of unbounded vertical fracture growth. Therefore, it is essential to accurately predict and control the vertical propagation of HFs. However, predicting fracture height is particularly challenging, as numerous field evidences suggest that the actual height of a HF often differs from what is predicted by state of the art hydraulic fracturing models (Smith & Montgomery, 2015). Microseismic and tiltmeter monitoring data from thousands of hydraulic fracturing treatments indicates that the

induced fractures are generally more constrained in the vertical direction and are longer laterally compared to theoretical predictions (Fisher & Warpinski, 2012; Flewelling et al., 2013).

The limitations of the vertical growth of HFs are traditionally thought to be a result of strong variation of in-situ stresses and material properties across rock formations (Jeffrey & Bunger, 2009; Simonson et al., 1978; van Eekelen, 1982; N. Warpinski et al., 1982; Xing et al., 2018), as well as interaction with pre-existing discontinuities in/across different rock formations (Teufel & Clark, 1984; N. R. Warpinski & Teufel, 1987; X. Zhang et al., 2007; J. Zhou et al., 2008). However, HFs more elongated horizontally than vertically have also been observed in homogeneous formations not exhibiting any increase in confining stress vertically that could explain this limited height growth (Ciezobka et al., 2018; Kohli & Zoback, 2021). We argue that—rock anisotropy—an intrinsic characteristic of sedimentary rocks has a first order impact on the shape of HFs and thus their ultimate vertical extent. In general, the anisotropic mechanical properties in rocks arise from the mineral foliation in metamorphic rocks, stratification in sedimentary rocks, and structural features in large rock masses (Cho et al., 2012; Hornby et al., 1994; Sone & Zoback, 2013). Unconventional hydrocarbon reservoirs are formed primarily in sedimentary basins, which have strong anisotropic material properties at a fine scale thanks to their deposition and diagenesis. More specifically, the anisotropy is caused by a common directional feature of sedimentary rocks—beds, which are generally sub-horizontal planes formed during the deposition of the sediments. Mechanical properties of sedimentary rocks, such as mudstones and shales, are found to vary substantially along different directions with respect to the bedding planes (Heng et al., 2015; Lu et al., 2021; Moukhtari, 2020; S. Zhang et al., 2018). They are widely modeled as a transversely isotropic material at the continuum scale (Johnston & Christensen, 1995; Jones & Wang, 1981; Moukhtari et al., 2020; Wang, 2002b). The anisotropic properties relevant to the propagation of fluid-driven HFs are mainly: (a) the elastic stiffness anisotropy (Cho et al., 2012; Meléndez-Martínez & Schmitt, 2016; Ong et al., 2016; Wang, 2002b; Wong et al., 2008), and (b) the tensile strength anisotropy (or equivalently, fracture toughness anisotropy in the context of Linear Elastic Fracture Mechanics) (Chandler et al., 2016; Cho et al., 2012; Lu et al., 2021; Nasseri et al., 2010; S. Zhang et al., 2018; Q. Zhou et al., 2023).

In recent decades, a growing body of research has investigated the growth of HFs in anisotropic rocks. Experimental studies have demonstrated the relative orientation between the fracture plane and the bedding largely affects the breakdown pressure in anisotropic rocks (Gehne et al., 2019, 2020; Q. Zhou et al., 2023). Numerical simulations of multiple hydraulic fracturing propagation have discovered that the fracture toughness anisotropy plays a critical role in determining the growth path and overall shape of the HFs (Benouadah et al., 2023; Sesetty & Ghassemi, 2018; Zia & Lecampion, 2020). A recent theoretical study has shown that the shape of a vertical HF that grows perpendicular to the bedding direction in a transversely isotropic rock differs remarkably from what would be expected in an isotropic rock, indicating a strong impact by the rock's anisotropic characteristics on the vertical containment of HFs at depth (Moukhtari et al., 2020).

Most laboratory hydraulic fracturing experiments in transversely isotropic rocks have focused on the initiation and early-time growth of HF, in which the fracture behavior is primarily governed by the release of the fluid volume stored in the injection system prior to initiation (Gehne et al., 2019, 2020; Tan et al., 2017; Y. Zhang et al., 2023; Zhao et al., 2022). Consequently, these HFs' initiation and propagation experiment are dominated by the toughness-dominated regime with a significant early-time compressibility effect (Abbas & Lecampion, 2013; Lecampion et al., 2017; Lu et al., 2017). Unfortunately, these conditions are not representative of all possible field conditions. While these results are instrumental in exploring the relationship between fracture initiation and rock anisotropy, limited experimental work has studied the stable growth of HFs in anisotropic rocks. Furthermore, the presence of weak bedding planes in sedimentary rocks like shale often leads to complex HF networks in lab-scale experiments (Tan et al., 2017; Y. Zhang et al., 2023; Zhao et al., 2022), making it difficult to distinguish the influence of intrinsic anisotropy of rocks from the governing effect of pre-existing beddings/discontinuities. For a comprehensive understanding of the impact of rock intrinsic anisotropy, including both the elastic stiffnesses anisotropy and fracture toughness anisotropy, on various naturally occurring and human-related HFs, a thorough analysis of the fracture propagation in anisotropic rocks across a wide parametric space covering different propagation regimes is imperative.

In this study, we bring together laboratory hydraulic fracturing experiments and numerical simulations to uncover the key factors that govern the vertical containment of HFs at depth in a transversely isotropic rock formation. The experimental setup utilizes acoustic monitoring techniques to recover the stable fracture propagation in a three-

dimensional (3D) configuration. Since our primary interest is the propagation of planar HFs in a plane perpendicular to its internal layering (a configuration of most practical relevance at depth), we minimize the fracture propagation in the foliation plane and avoid creating complex fracture networks (which is typically favored at shallow depth/low confining stresses).

2. Materials and Methods

2.1. Rock Anisotropy Characterization

All hydraulic fracturing experiments are carried out on Del Carmen slate specimens. The Del Carmen slate is a finely laminated metamorphic rock with an extremely small porosity from La Baña, León, North-West Spain. Mineral composition and organic content of the Del Carmen slate are determined through X-ray Powder Diffraction analysis (Moukhtari, 2020). We observe a concentration of 35.7% of laminated silicates (in particular chlorite and mica), 43.61% of quartz, and some minor constituents such as plagioclases (12.84%) and feldspars (3.15%). In general, transverse isotropy in slate is characterized by its foliation—fine-grained parallel layers of minerals aligned due to the intense heat and pressure of metamorphism. In contrast to sedimentary rocks which often have a length-scale of layering comparable to the sample size ($O(10^2)$ mm in this study), the small thickness of the foliation layers in the Del Carmen slate ensures a relatively homogeneous transversely isotropic structure across the specimen. Therefore, we will use the experimental data as an analog for large-scale (10^2 m) in-situ HFs propagating in sedimentary basins.

The slate exhibits two typical transversely isotropic properties relevant to the growth of mode I HFs: (a) five independent elastic stiffnesses C_{ij} (or equivalently, the corresponding anisotropic plane-strain near-tip elastic moduli $E'(\theta)$ in Figure 1a (Chertov, 2012; Laubie & Ulm, 2014; Moukhtari et al., 2020), the engineering elastic parameters (Meléndez-Martínez & Schmitt, 2016; Ong et al., 2016; Wong et al., 2008), and Thomsen parameters (Thomsen, 1986)), and (b) an anisotropic variation of the critical energy to propagate a fracture as function of the fracture growth direction with respect to the plane of isotropy (bedding plane in sedimentary rocks and foliation plane in metamorphic rocks), $K_{Ic}(\theta)$ (Figure 1a).

For a planar HF growing perpendicular to horizontal layering (Figure 1a), we define ($\boldsymbol{e}_1$, $\boldsymbol{e}_2$) as the plane of material isotropy, and $\boldsymbol{e}_3$ is the axis of rotational symmetry (normal to the foliation planes). At an arbitrary point along the fracture front, its propagation direction is characterized by the angle θ between the unit outward normal vector to the fracture front $\left(\boldsymbol{e}'_1\right)$ and the foliation plane ($\boldsymbol{e}_1$), $\theta = (\widehat{\boldsymbol{e}'_1,\boldsymbol{e}_1})$. Therefore, we define the local coordinate system $\left(\boldsymbol{e}'_1,\boldsymbol{e}'_2,\boldsymbol{e}'_3\right)$ with $\boldsymbol{e}'_1$ corresponding to the direction of propagation of local fracture front, $\boldsymbol{e}'_3$ being parallel to fracture front, and $\boldsymbol{e}'_2 = \boldsymbol{e}_2$. The five independent elastic stiffnesses C_{ij} of the transversely isotropic slate defined by the global (material) coordinate system are determined by ultrasonic measurements of compressional- and shear-wave velocities (Tsvankin, 2012; Wang, 2002a) (see their values given in Appendix A). To quantify the influence of transversely isotropic elastic stiffnesses, we adopt the definition of the plane-strain near-tip elastic modulus $E'(\theta)$ (Moukhtari et al., 2020) governing the elastic deformation of semi-infinite fracture propagating at angle θ from the material isotropy plane in transversely isotropic rocks (see Figure 1c for a sketch):

$$E'(\theta) = \frac{2M(\theta)C'_{22}C'_{66}}{\sqrt{C'_{22}C'_{11}}}$$
$$M(\theta) = \left(\sqrt{C'_{22}C'_{11}} + C'_{12}\right) \times \left(\frac{\sqrt{C'_{22}C'_{11}} - C'_{12}}{C'_{22}C'_{66}\sqrt{C'_{22}C'_{11}} + C'_{12} + 2C'_{66}}\right)^{1/2} \quad (1)$$

in which C'_{ij} denote the components of rotated (by angle θ) transversely isotropic stiffness tensor $\mathbf{C}'$. The values of C'_{ij} are computed using a transformation matrix $\mathbf{T}$ given in Appendix A. $E'(\theta)$ in Equation 1 is the elastic modulus (due to transverse isotropy) governing the elastic deformation of a mode I semi-infinite fracture propagating along a direction oriented at an angle θ with respect to the material coordinate system (Hirth & Lothe, 1982; Moukhtari et al., 2020). The value of $E'(\theta)$ decreases monotonically (in the case of slate studied in this work) with θ ($0 \le \theta \le \pi/2$), with the two limiting values along $\theta = 0$ $\left(\boldsymbol{e}'_1 = \boldsymbol{e}_1\right)$ and $\pi/2$ $\left(\boldsymbol{e}'_1 = \boldsymbol{e}_3\right)$:

$$E'_1 = E'(\theta = 0) = 107.5 \text{ GPa}$$

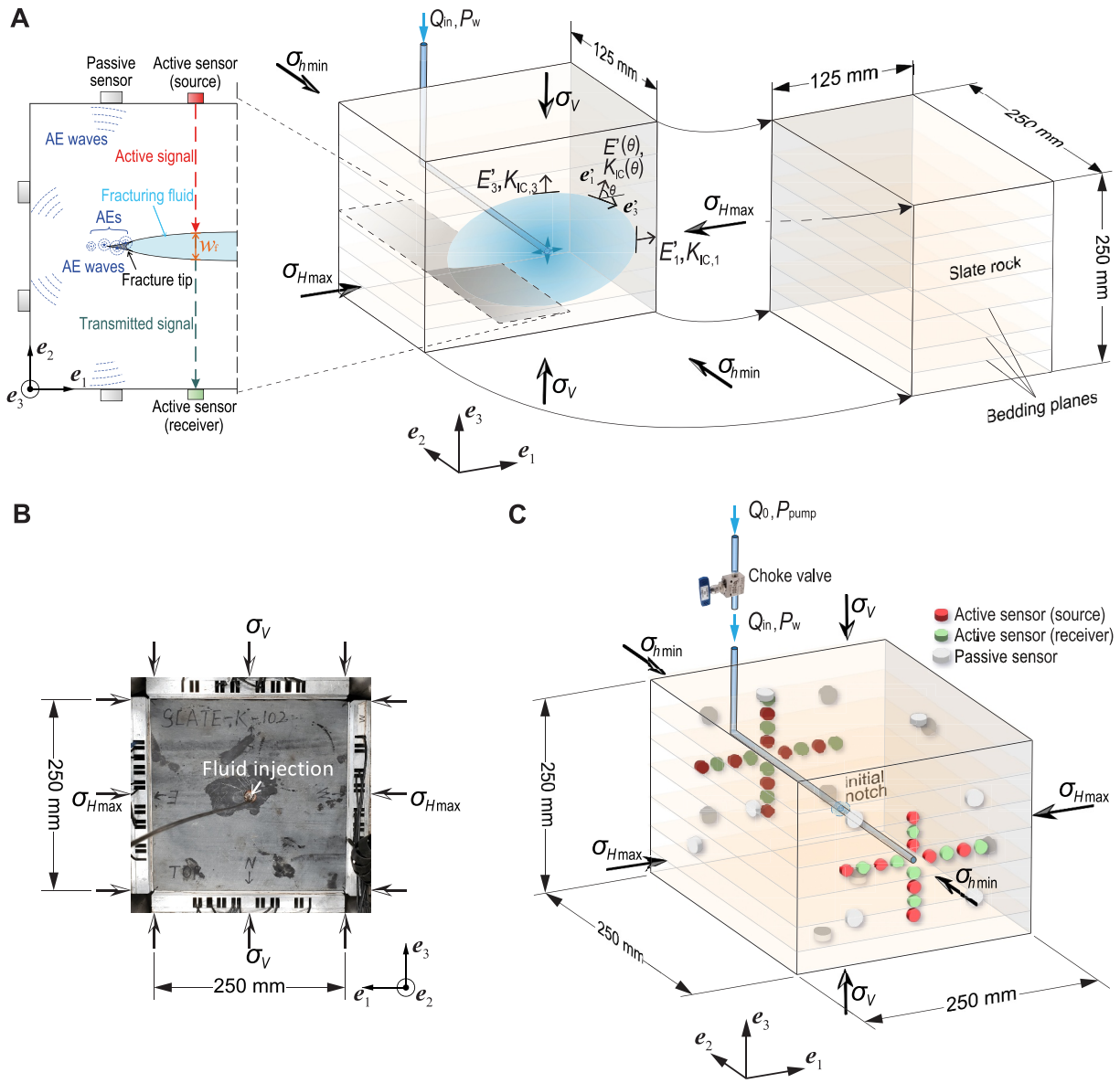

Figure 1. (a) Cross sectional view of a propagating hydraulic fracture (HF) in the experiments on an anisotropic slate (right) with a conceptual sketch of the passive (acoustic emissions) and active (wave transmission) acoustic monitoring system (left). The experiments are designed to mimic a vertical HF propagating in a layered rock formation at depth. (b) Photograph of the Carmen slate block under confinements. (c) Active and passive acoustic sensor layout.

$$E'_3 = E'\left(\theta = \frac{\pi}{2}\right) = 97.2 \text{ GPa}$$

Next, the fracture toughness of the slate is measured by three-point loading on semicircular bending specimens (Kuruppu et al., 2014). Samples are prepared in two orientations with respect to the foliation planes to measure two extreme values of K_{Ic} along the parallel-to-foliation ($K_{Ic,1}$ = 2.5 MPa$\sqrt{m}$) and perpendicular-to-foliation ($K_{Ic,3}$ = 3.5 MPa$\sqrt{m}$) directions, respectively. The direction dependent anisotropic fracture toughness, $K_{Ic}(\theta)$, used in our analysis is then determined by a specific form (Moukhtari, 2020):

$$K_{\mathrm{Ic}}(\theta) = K_{\mathrm{Ic},3}\frac{E'(\theta)}{E'_3}\left[\sin^2\beta + \left(\frac{K_{\mathrm{Ic},1}E'_3}{K_{\mathrm{Ic},3}E'_1}\right)^4\cos^2\beta\right]^{\frac{1}{4}} \quad (2)$$

in which $\beta = \arctan\left(\left(\frac{K_{\mathrm{Ic},1}E'_3}{K_{\mathrm{Ic},3}E'_1}\right)^2\tan\theta\right)$. Equation 2 ensures an exact elliptical shape for a planar mode I fracture (normal to the plane of isotropy) under uniform loading acting on the fracture plane (Moukhtari et al., 2020). This expression also enables the derivation of explicit solution of the fracture shape in the toughness-dominated regime (discussed in Section 4). Similarly, the value of $K_{\mathrm{Ic}}(\theta)$ increases monotonically from 0 ($K_{\mathrm{Ic},1} = K_{\mathrm{Ic}}(\theta = 0) = 2.5$ MPa$\sqrt{\mathrm{m}}$) to $\pi/2$ ($K_{\mathrm{Ic},3} = K_{\mathrm{Ic}}(\theta = \pi/2) = 3.5$ MPa$\sqrt{\mathrm{m}}$).

We will use both ratios of E'_3/E'_1 and $K_{\mathrm{Ic},3}/K_{\mathrm{Ic},1}$ to examine the impact of rock anisotropy in (a) elastic stiffnesses and (b) fracture toughness on the growth of the planar HF in different propagation regimes.

2.2. Hydraulic Fracture Propagation Regimes

Hydraulic fracture growth in low permeability isotropic material is well known to be governed by the relative influence of the energy dissipated in fracture creation with respect to the energy dissipated in viscous fluid flow in the fracture (Bunger & Detournay, 2008; Detournay, 2004; Savitski & Detournay, 2002). It results in two distinct regimes of propagation: a toughness-dominated regime where the energy spent in fracture creation dominates, and a viscosity-dominated regime where fluid viscous energy dissipation dominates. Our aim is to study the impact of transverse isotropy on the overall shape of HF propagating in both types of propagation regimes.

The relative influence of these two dissipative mechanisms (surfaces creation and viscous flow) on HF growth can be quantified by a dimensionless fracture toughness $\mathcal{K}_m$ obtained from scaling considerations (Bunger & Detournay, 2007; Detournay, 2004; D. I. Garagash, 2009; Lecampion et al., 2017; Lu et al., 2017; Savitski & Detournay, 2002). In fact, it is computed as the square root of the ratio of fracture creation to viscous flow energy dissipation. Accounting for a time-varying injection from a point source, it is given by (D. I. Garagash, 2009)

$$\mathcal{K}_m(t) = \frac{K_{\mathrm{Ic}}t^{5/18}}{E'^{13/18}\mu'^{5/18}V_{\mathrm{in}}(t)^{1/6}} \quad (3)$$

where K_{Ic} is the fracture toughness, $E' = E/(1-\nu^2)$ represents the plane-strain elastic modulus, $\mu' = 12\mu$ with μ the dynamic viscosity of the injection fluid, and $t = T - T_0$ where T and T_0 are the absolute and fracture initiation time, respectively. $V_{\mathrm{in}}(t) = \int_0^t Q_{\mathrm{in}}(\tau)\mathrm{d}\tau$ represents the total volume of fluid in the fracture, where Q_{in} is the fluid influx into the fracture accounting for wellbore compressibility (Liu & Lecampion, 2022a; Lu, Momeni, & Lecampion, 2022). A radial HF in an isotropic material (Savitski & Detournay, 2002) grows in the toughness-dominated regime for $\mathcal{K}_m \geq 1.1$, and in the viscosity-dominated regime when $\mathcal{K}_m \leq 0.32$. We consider any value ranging from 0.32 to 1.1 as a transitional regime between the two limiting values.

In Equation 3, E' and K_{Ic} are both constant for an isotropic medium. Similar scaling laws hold for a transversely isotropic rock (Dontsov, 2019; Moukhtari et al., 2020). It is noteworthy that both values of E' and K_{Ic} evolve monotonically with the direction angle θ in a transversely isotropic medium. Hence, for a planar HF growing at a given time t, there exist an upper limit, $\mathcal{K}_m^{(\boldsymbol{e}_3)} = \frac{K_{\mathrm{Ic},3}t^{5/18}}{E'^{13/18}_3\mu'^{5/18}V_{\mathrm{in}}(t)^{1/6}}$ (corresponding to fracture growth along $\boldsymbol{e}_3$ direction), and a lower limit, $\mathcal{K}_m^{(\boldsymbol{e}_1)} = \frac{K_{\mathrm{Ic},1}t^{5/18}}{E'^{13/18}_1\mu'^{5/18}V_{\mathrm{in}}(t)^{1/6}}$ (governs the propagation along the $\boldsymbol{e}_1$ direction).

2.3. Extensive Acoustic Monitoring Methods to Capture Laboratory Hydraulic Fracture Evolution

A total of four hydraulic fracturing experiments are carried out on cubic blocks of Del Carmen slate in a true-triaxial load frame (Figure 1). The slate specimens used in the experiments are 250 × 250 × 250-mm cubic blocks (Figure 1b). A surface grinder is employed in the preparation of the blocks to ensure precision-ground and parallel surfaces. The specimens have an average length of 248.5 mm (±1.5 mm) along both $\boldsymbol{e}_1$ and $\boldsymbol{e}_2$ directions, and 244.3 mm (±1 mm) along the $\boldsymbol{e}_3$ direction. All samples are prepared with an axisymmetric notch (10-mm radius) that emanates from the center of the horizontal wellbore with 8-mm radius (see more details in Liu and Lecampion (2022a)). The fracture is driven by the injection of different Newtonian fluids in the axisymmetric

Table 1
Summary of Testing Conditions

Test ID	Q_0 (ml/min)	μ (Pa s)	σ_v (MPa)	$\sigma_{H\max}$ (MPa)	$\sigma_{h\min}$ (MPa)	Test duration $T_{\exp}$ (s)	Regime
K1	0.04	0.11	20	13	0.5	82	Toughness-dominated
T2	0.08	0.617	20	13	0.5	55	Transitional
M3	0.15	25.4	20	13	0.5	558	Viscosity-dominated
M4	0.15	25.4	20	13	0.5	508	Viscosity-dominated

notch through a wellbore drilled in the center of the specimen. The injection system is separated into two parts by a choke valve: (a) the upstream that starts from the pump and ends before the valve (under constant pumping rate, Q_0, and pump pressure, P_{pump}), and (b) the downstream that consists of the fluid passing through the valve and flowing into the fracture (with a fluid influx of Q_{in} and wellbore pressure of P_{w}). Three types of fluid are used as the injection fluid: (a) Mixture of glycerol and water is used in K1 to facilitate fracture growth in a toughness-dominated regime, (b) T2 uses 99% glycerol for maintaining the propagation in a transition regime, and (c) glucose is used in M3 and M4 to target for the viscosity-dominated regime hydraulic fracturing growth. The dynamic viscosity of the fluid, μ, is measured before each experiment to ensure accurate values are reported at the time of testing (Table 1). The foliation plane is set to be orthogonal to the fracture plane to replicate the in-situ condition of a vertical HF growth at depth in sedimentary basins (Figure 1a). We apply a sufficiently large vertical stress, σ_v (normal to the foliation plane), in a true triaxial frame with the three confining stresses, σ_v, $\sigma_{H\max}$, and $\sigma_{h\min}$ given in Table 1. This setup maximizes the vertical extent of the created fracture and avoid any deviation of the fracture into a foliation plane.

Extensive acoustic measurements, via both passive and active acoustic methods, are used to image the HF propagation. The appearance of micro-cracks adjacent to the macro-scale fracture is accompanied by the emission of transient elastic waves due to the release of strain energy, which is referred to as acoustic emissions (AEs) (Chang & Lee, 2004; Hampton et al., 2018, 2019; Lockner, 1993; Lu et al., 2021; Shah & Labuz, 1995). Our passive acoustic monitoring network consists of 16 piezoelectric sensors mounted on all six surfaces of the block as shown in Figure 1c. Throughout the experiments, each of the 16 VS150-M Vallen resonant (at 150 KHz) piezoelectric sensors, covering frequencies from 100 KHz to 1 MHz, records AEs in a continuous mode with a sampling rate of 10 MHz. The sensors are installed in six platens surrounding the specimen. The proper contact between sensors and specimen is provided by springs placed behind each sensor in platens and a highly viscous coupling gel. The 3D hypocenter location of the AE events are obtained by a semi-automatic algorithm using a modified Time Difference Of Arrival method (Kundu, 2014; Momeni et al., 2021), with the compressional-wave velocities of the rock at different orientations measured for intact specimens. This method includes signal pre-processing, signal detection at each sensor, event association, signal feature extraction in both time and frequency domains, and a two-step grid search for potential hypocenter location. The relative magnitudes of the AEs are estimated based on wave amplitudes and source-to-receiver distance (Zang et al., 1998).

In parallel to passive monitoring, an active acoustic array consisting of 16 source-receiver sensor pairs allows us to track the evolution of the macro-scale fracture. These source-receiver pairs, mounted on two opposite vertical faces parallel to the HF plane (Figures 1a and 1c), enable estimation of the fracture width at 16 locations via an analysis of transmitted waves with a 90° incident angle. In a three-layer geometry (rock-fluid-rock) as shown in Figure 1a, the thickness of the fluid layer (i.e., fracture width), w_{f}, is evaluated by matching the spectrum of the transmitted signals traveling between two facing source-receiver transducers with the predicted values (Groenenboom & Fokkema, 1998; Kovalyshen et al., 2014; Liu & Lecampion, 2022a; Liu et al., 2020). More details of the calculations are provided in Appendix B. Repetitive acoustic surveys are carried out at a fixed time interval (every 10 s), using a total of 32 Controltech resonant (at 750 KHz) piezoelectric compressional-wave transducers (16 source-receiver pairs) with frequency coverage from 100 KHz to 4 MHz. Each survey consists of 50 source excitations using the Ricker function with a peak frequency of 750 KHz that are stacked to improve the signal-to-noise ratio, and w_{f} is computed at every survey. More details of the acoustic monitoring methods are provided in Appendix B.

The simultaneous passive and active acoustic monitoring provide a wealth of information on both micro-fracturing and macro-scale HF width evolution. Integrating these methods allows to successfully capture the 3D evolution of HF growth in these experiments.

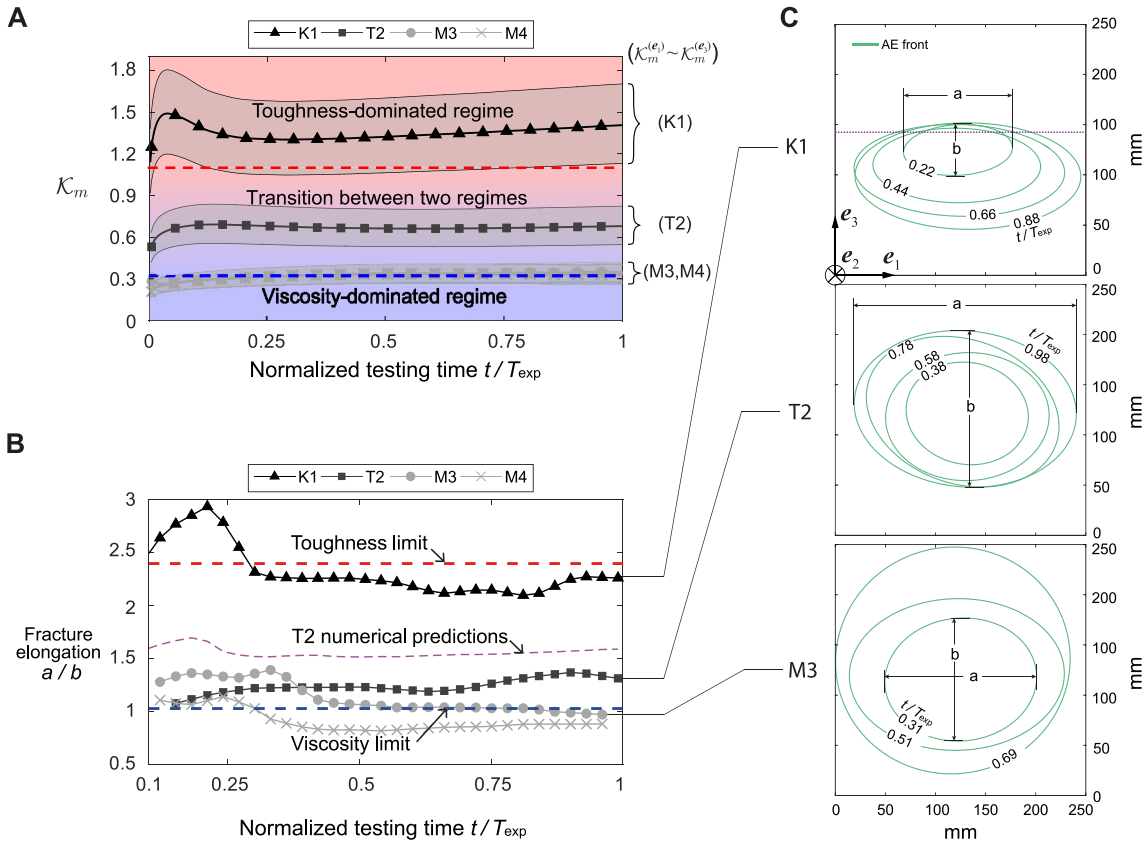

Figure 2. (a) Evolution of the two limits of dimensionless toughness, $\mathcal{K}_m^{(e_3)}$ (upper limit $\mathcal{K}_m$) and $\mathcal{K}_m^{(e_1)}$ (lower limit $\mathcal{K}_m$), with normalized testing time, t/T_{exp}, where T_{exp} is defined as the total test duration in each experiment. The average $\mathcal{K}_m$ is also plotted using E' and K_{Ic} computed as $E' = \left(E'_1 + E'_3\right)/2$, $K_{Ic} = (K_{Ic,1} + K_{Ic,3})/2$, with $E'_1 = E'(\theta = 0)$, $E'_3 = E'\left(\theta = \frac{\pi}{2}\right)$, $K_{Ic,1} = K_{Ic}(\theta = 0)$, and $K_{Ic,3} = K_{Ic}\left(\theta = \frac{\pi}{2}\right)$. (b) a/b measured in all tests plotted together with reference values in limiting cases in both toughness- and viscosity-dominated regimes and simulation results of the transition test. (c) Elliptical shape of the hydraulic fractures reconstructed using acoustic emission data in the toughness-dominated (K1), transition (T2), and viscosity-dominated (M3) experiments. The most elliptical shape is observed in the toughness-dominated regime, and a radial hydraulic fracture (no elongation) is seen in the viscosity-dominated test.

2.4. Numerical Model

The planar 3D open-source HF simulator—Pyfrac (Moukhtari et al., 2020; Zia & Lecampion, 2020)—is used to simulate the growth of a fluid driven fracture. It has been extensively validated against both analytical solutions and experiments performed in isotropic materials. The model I HF is set to propagate on the plane perpendicular to the isotropy plane ($\boldsymbol{e}_1\boldsymbol{e}_3$-plane). The quasi-static fracture propagation is driven by the injection of a Newtonian fluid with dynamic viscosity, μ, at the central borehole with time varying rate, $Q_{in}(t)$. Both elastic stiffnesses anisotropy 1 and fracture toughness anisotropy 2 are considered through the constitutive relation and the propagation condition. The input parameters in the numerical model, including the rock and fluid properties, minimum horizontal confining stress, σ_{hmin}, and the injection rate history $Q_{in}(t)$, are set to be the exact same values as in the laboratory experiments.

3. Results

3.1. Fracture Elongation Induced by Material Anisotropy

The experimental conditions are summarized in Table 1. By varying the fluid injection conditions (fracturing fluid viscosity and injection rate), we aim for specific propagation regimes (toughness-dominated, viscosity-dominated, and transition regimes) in different experiments. Figure 2a gives the evolution of both $\mathcal{K}_m^{(e_3)}$ (upper limit $\mathcal{K}_m$) and $\mathcal{K}_m^{(e_1)}$ (lower limit $\mathcal{K}_m$) with normalized testing time, t/T_{exp}. Consequently, the front behavior (tip asymptote) at any arbitrary orientation (θ) along the planar fracture should follow a characteristic toughness $\mathcal{K}_m$

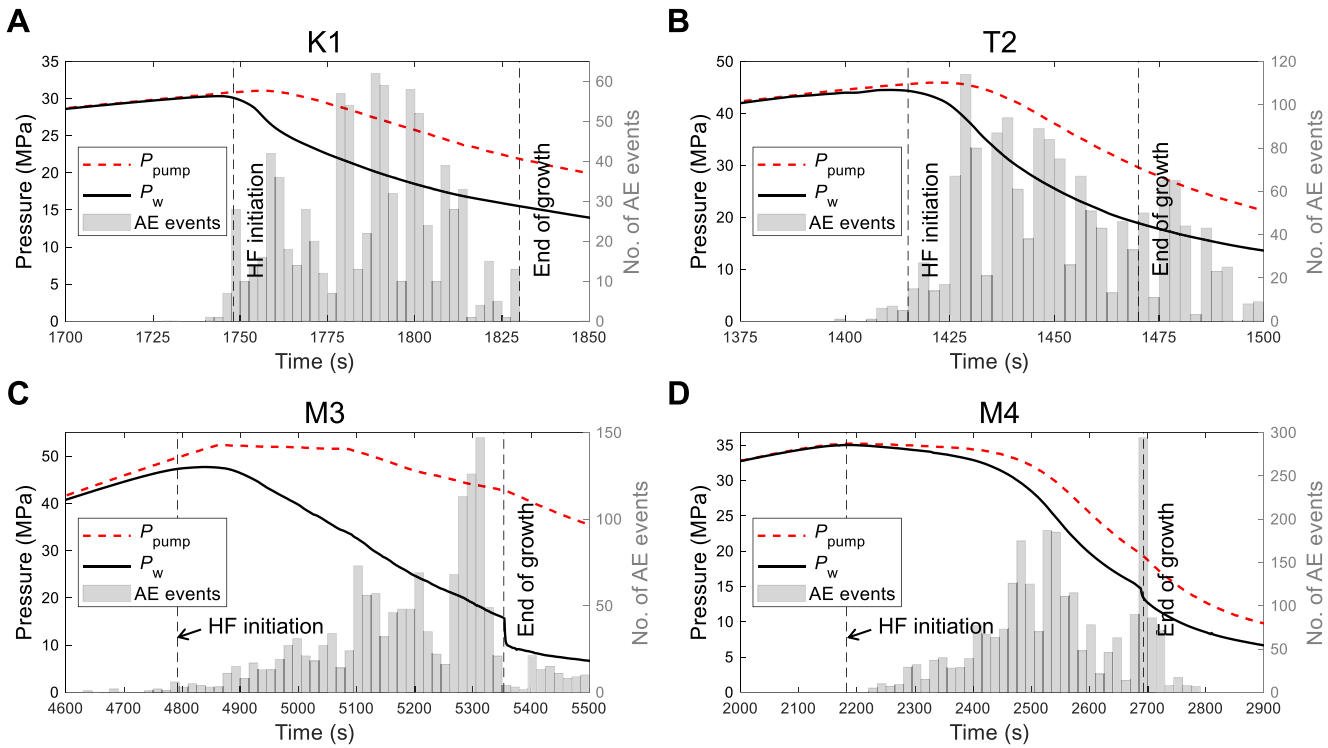

Figure 3. Evolution of pump pressure, P_{pump}, wellbore pressure, P_w, and number of acoustic emissions (AEs) with time of all experiments. The time of hydraulic fracture (HF) initiation and end of growth are determined by clear signs such as pressure change, and the location and number of AEs. In both M3 and M4, very few AEs were detected in the first ~100 s after the fracture initiation (initiation time determined by change in slope of the wellbore pressure as fluid starts to flow into the HF). Therefore, this period of time was disregarded in the analysis of AE front evolution.

between the two limits (shaded area in Figure 2a for each test). In all experiments, we find that both limits of $\mathcal{K}_m$ primarily fall into the same category throughout the lifetime of the specimens, namely, the toughness-dominate, viscosity-dominated, or transition regime. Based on the scaling analysis outlined in Section 2.2, two experiments were performed under viscosity-dominated regime (hereafter denoted as M3 and M4), experiment K1 was in toughness-dominated regime, and T2 is considered to be in the transition regime. It is reasonable to infer that these test results represent typical fracture behaviors in their corresponding regimes. For convenience, we will use the average value of both properties, $E' = \left(E'_1 + E'_3\right)/2$ and $K_{Ic} = (K_{Ic,1} + K_{Ic,3})/2$, for computing a representative $\mathcal{K}_m$ in the following analysis.

The pressure and AE events histories in all four experiments are plotted in Figure 3. First, we focus on the toughness-dominated regime test, K1. AE data is collected throughout the experiment. A majority of the events are concentrated along the final fracture plane as the AE hypocenters (Figure 4a) overlap with the fracture plane highlighted in the post-test photograph of sample surface (also confirmed by the AE density plot in Figure S1 in Supporting Information S1). The upward growth of the HF along positive $\boldsymbol{e}_3$ direction (perpendicular-to-foliation) was stopped by a specific foliation plane located ~2 cm above the wellbore (which was visible on the specimen surfaces before the test when wetted). Although there was no interruption of the HF by any foliation plane below the wellbore, the fracture plane did not reach the bottom face. On the contrary, we observe larger fracture length along $\boldsymbol{e}_1$ direction (parallel-to-foliation), as the fracture eventually extended to the full length of 250 mm in $\boldsymbol{e}_1$ direction. The event locations projected on the 2D $\boldsymbol{e}_1\boldsymbol{e}_3$-plane in Figure 4c also suggest that micro-cracking extends further along the parallel-to-foliation direction compared to the perpendicular-to-foliation direction.

This finding is consistent with numerical and analytical studies that suggest an ellipse-like shape for a fluid driven fracture propagating in a transversely isotropic rock (Bessmertnykh & Dontsov, 2018; Dontsov, 2019; Laubie & Ulm, 2014; Moukhtari et al., 2020). Following these previous works, and considering that AEs generally take place in the adjacent areas of the growing fracture front, it is sensible to assume that the frontier formed by the AEs also expands with an elliptical shape. This assumption enables us to reconstruct a generalized AE front by

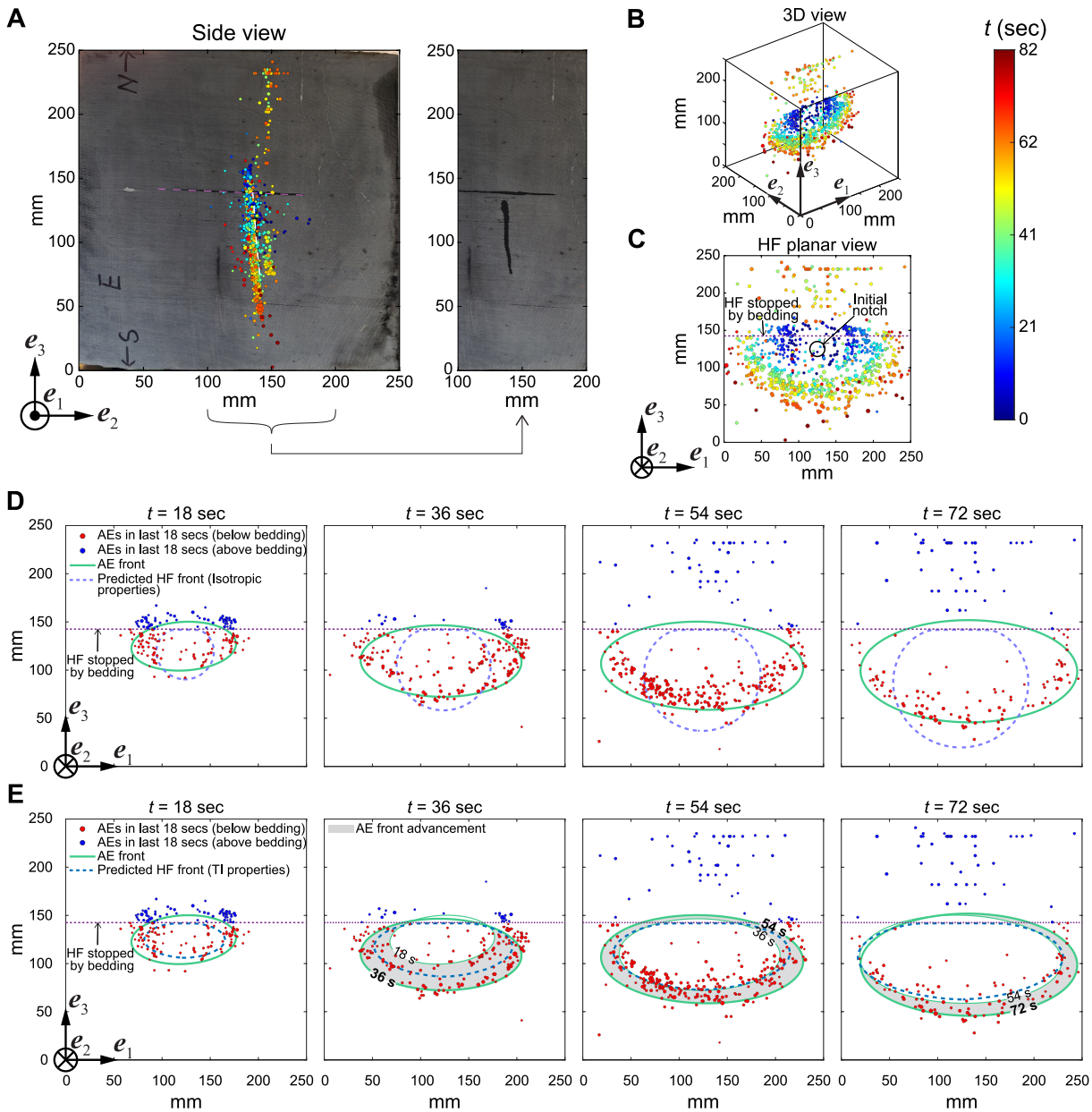

Figure 4. Experimental and simulation results of test K1. (a) Hypocenter location of the acoustic emissions (AEs) plotted on $\boldsymbol{e}_2\boldsymbol{e}_3$-plane, superimposed on the post-test photograph of the sample surface, with the event occurrence time and magnitude indicated by the color and size of the circles, respectively. The final hydraulic fracture (HF) plane (white dashed line) is seen to be completely stopped by a visible foliation plane (purple). (b, c) 3D and $\boldsymbol{e}_1\boldsymbol{e}_3$-planar view of the event hypocenter locations. (d) Four snapshots taken in different times demonstrating the comparisons between the reconstructed AE front and predicted fracture front assuming HF growth in an isotropic medium (projected on the same 250 × 250-mm $\boldsymbol{e}_1\boldsymbol{e}_3$-plane as in (c)). Events that occur within the last $\Delta t = 18$ s before the time of every snapshot are also plotted. In the elliptical front reconstruction for K1, the events located above the foliation plane are disregarded since the HF was stopped by the weak plane, and these events are considered as pure micro-cracks that do not coalesce into the macro-scale fracture. (e) Comparisons between AE front and predicted fracture front obtained from the HF solver considering a transversely isotropic medium. The gray area highlights the advancement of the AE front between two snapshots.

solving a least-squares problem (Appendix B) to fit the best ellipse for the outermost events that occur within a given time interval (green ellipse in Figure 4d). Four snapshots of the reconstructed fronts are shown in Figure 4d. The major and minor semi-axes are found to be aligned generally with the $\boldsymbol{e}_1$ and $\boldsymbol{e}_3$ directions, implying a clear elongation of the HF growth along the parallel-to-foliation direction. To investigate the elongation of the HF, we measure the ratio of the fracture extent along $\boldsymbol{e}_1$ direction, a, over its value along $\boldsymbol{e}_3$ direction, b. As shown in Figure 4c, a increases to as high as ~3 times of b, indicating a significant elongation of the HF along the parallel-to-foliation direction.

To demonstrate that such elongated fracture growth is due to the rock's transversely isotropic characteristics, instead of being caused by the specific foliation plane interrupting the fracture propagation, the experimental results are compared with numerical predictions by two models: an isotropic model and a transversely isotropic one for the rock. These simulations are carried out using an extensively verified planar 3D hydraulic fracturing solver, Pyfrac (Moukhtari et al., 2020; Zia & Lecampion, 2020). The first model solves the problem of a HF propagating in an isotropic medium with a uniform fracture toughness (Zia & Lecampion, 2020) (independent of the propagation direction). To prevent the fracture from advancing across the observed specific foliation plane, a jump in fracture toughness is imposed at that location, to a level that is much higher than the uniform fracture toughness of the medium. As a result, the fracture initially grows in a radial shape until hitting the foliation plane (Figure 4d). As its propagation is partially disrupted by the foliation plane, its center begins to shift downward in an effort to maintain a somewhat radial shape, and eventually reaches the bottom surface prior to hitting both vertical faces. Substantial discrepancies are found between the numerical predictions and the reconstructed AE fronts. To summarize, for an isotropic rock, the arrest of the propagation of a planar HF on one side would enhance, instead of suppressing, its growth in the opposite direction. In the second model, we account for the transversely isotropic features of the medium (Moukhtari et al., 2020; Zia & Lecampion, 2020). More specifically, the rock's elastic deformation and resistance to creation of new fracture surfaces induced by fluid pressure now depend on five transversely isotropic elastic stiffnesses, as well as the anisotropic fracture toughness. Detailed comparisons between the AE fronts and the predicted fracture fronts provided in Figure 4e reveal that: (a) The AE front constantly propagates ahead of the HF front; (b) both fronts advance at roughly the same pace; (c) the AE clusters are scattered initially and become more concentrated in the predicted fracture front region. The elliptical AE front has a better agreement with the predicted fracture front when accounting for transverse isotropy compared to the radial shape as typically observed in HFs in an isotropic medium. We will use the transversely isotropic model as numerical predictions for HF growth hereafter.

3.2. Effect of Viscous Fluid Dissipation on Fracture Elongation

Next, we demonstrate the fracture growth in experiments under other regimes: experimental results for the transition regime (T2) and the viscosity-dominated regime tests (M3 and M4) are displayed in Figures 5 and 6 and Figure S2 in Supporting Information S1, respectively. In all experiments, the final fracture plane remains vertical with little inclination (as illustrated by the AE density plots in Figure S1in Supporting Information S1). The evolution of the AE frontier in all tests indicates that: (a) the effect of rock anisotropy is most significant in the toughness-dominated regime, which evidently promotes fracture containment in the perpendicular-to-foliation direction; (b) as the propagation regime transitions toward the viscosity-dominated regime (decreasing $\mathcal{K}_m$), the reconstructed front becomes less elliptical, and the AEs are found to be more scattered across the entire fracture plane. Post-test visual examination on the fracture path confirms larger vertical growth in the two viscosity-dominated tests compared to the toughness-dominated and transition tests.

Notably, the predicted fracture width in T2 converges to the measured one at multiple locations near the wellbore (Figure 5e), confirming that the HF was centered at the wellbore and remained vertical during the experiment. In the viscosity-dominated tests, regardless of the scattering in the events, it is seen that the AE front matches well with the predicted fracture front throughout the lifetime of both specimens.

3.3. Estimation of Fluid Lag in Viscosity-Dominated Experiments

The fracture width in M3 recorded by four source-receiver pairs (see locations of all pairs in Figure 7) increases together with the numerical solution in both early and late times. However, a drop at an intermediate time in most measurement locations (#10, 11, and 15) is observed. This phenomenon is possibly associated with the occurrence of a fluid lag—as often observed in viscosity-dominated HF tests (Bunger & Detournay, 2008). Strong elasto-hydrodynamics coupling in the near-tip region of a HF induces cavitation such that the fluid front lags behind the fracture tip (D. Garagash & Detournay, 2000). Consequently, the acoustic signal cannot travel through the HF when it hits this near-tip nonwetted zone, which leads to erroneous estimations of the fracture opening (Liu & Lecampion, 2022b). As a result, the width evolution in the viscosity-dominated regime tests likely experiences three phases (Figure 7d): I. Once the fracture tip arrives at the location that intervenes with the active signal, the two fracture faces start to separate as the width is observed to be increasing with time. During this phase, the fracture faces are still bonded by inter-granular forces, such that an interface, filled with deformed rock particles, is formed. The acoustic signals are still able to travel through this bonded interface. Accordingly, we see increase in the

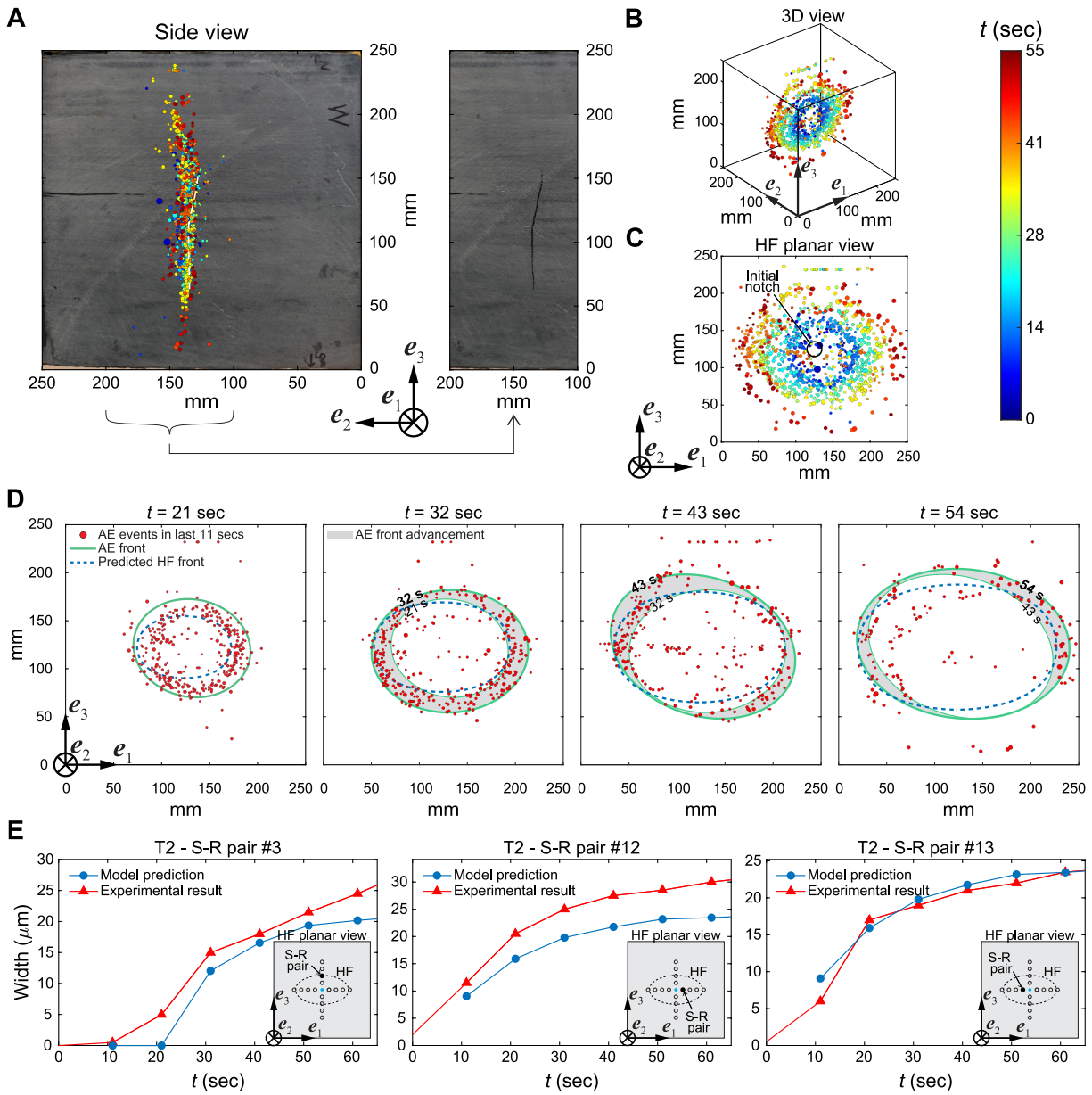

Figure 5. Experimental and simulation results for the T2 test (transition regime). (a–d) Post-test photograph, 3D and $\boldsymbol{e}_1\boldsymbol{e}_3$-planar view of the event hypocenters compared with model predictions. (e) Width evolution at source-receiver (S–R) pairs #3, 12, and 13 in T2, with sensor locations indicated on the $\boldsymbol{e}_1\boldsymbol{e}_3$-plane. The width is 5–10 μm larger than the model prediction. Such discrepancy can be explained by the fact that elastic stiffnesses used in numerical modeling are based on ultrasonic wave-speed measurements, which, in general, are higher than their quasi-static values. The numerical solver thus likely underestimates the fracture width due to overestimation of the elastic stiffness constants.

fracture width in this rock-solid interface-rock geometry. II. The two fracture faces become fully debonded when its width reaches 20–30 microns, while the fluid front is still lagging behind. The appearance of the lag zone hinders wave transmission, and results in erroneous values in the width evaluation as huge drops are seen during this phase. We consider the tip of region II as the actual fluid lag front (which differs from the AE front), as the fracture is fully open after the width surpasses certain threshold. III. Finally, the lagging fluid front advances to this region and occupies the previously void space, which reopens the pathway for the acoustic signals to travel through the intermediate fluid layer. Width estimation regains its accuracy since wave transmission is restored in this phase.

To quantify the size of the fluid lag, we evaluate the strength of the transmitted signal for a given source-receiver pair #*i* at time *t*, $I_i(t)$, defined as (Liu et al., 2020)

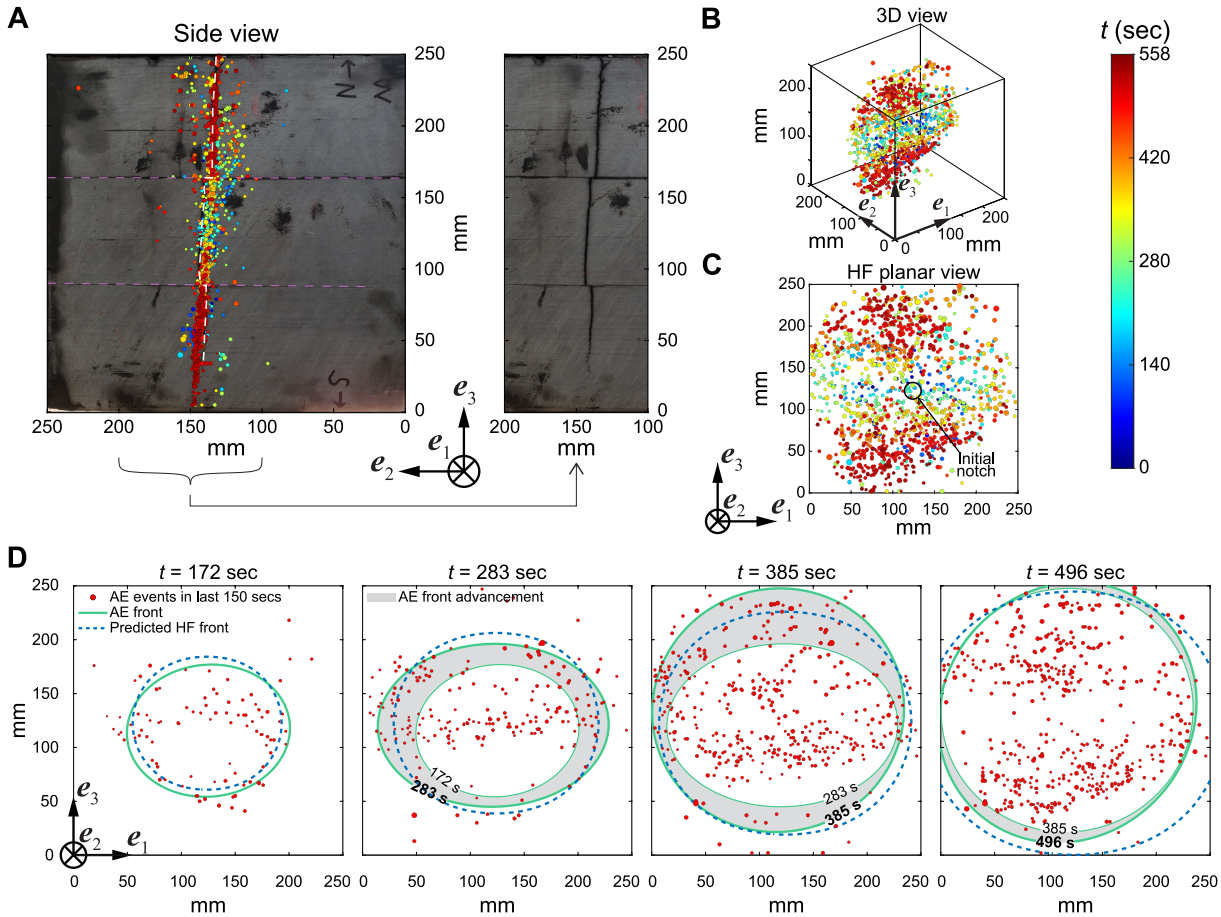

Figure 6. Experimental and simulation results of the M3 test (viscosity-dominated regime). (a–d) Post-test photographs, 3D and $\boldsymbol{e}_1\boldsymbol{e}_3$-planar view of the event hypocenters compared with model predictions.

$$I_i(t) = \int_{t-\Delta t}^{t+\Delta t} u^2(t) \tag{4}$$

in which u is a low-pass filtered (at 2 MHz) waveform that is cropped by a tapered Hamming window centered on the interest time (Δt = 7 μs). A reference signal prior to fracture initiation is then used to compute the ratio, $\left(I_i(t)/I_i^{ref}\right)^{1/2}$. This ratio can be considered as the attenuation in the transmitted signals of a specific source-receiver pair. The signals generally experience substantial attenuation upon the arrival of the fracture front and regains its overall trend as soon as the fluid front advances to this location (Liu & Lecampion, 2022b). Figure 7b shows the signal attenuation is consistent with the width analysis (Figure 7a) in discerning the three phases at the tip region. The signal strength follows an overall downward trend with time. However, its value suddenly drops when the void crack tip (due to fluid lag) arrives, followed by significant fluctuation and deviation from the downward trend until the arrival of the fluid front (onset of phase III). Based on these observations, we plot both AE fronts at the start and the end of phase II determined in Figures 7a and 7b. Assuming (a) elliptical fracture growth centered at the injection well and that (b) the fluid lag front advances at the same pace as the AE front, we can estimate the size of the fluid lag using the distance between two fronts (Figure 7c). In test M3, the fluid lag size varies from 19 to 47 mm at three different locations (source-receiver pairs 10, 11, and 15). It is important to note that this analysis provides a first-order estimate of the fluid lag size, and errors can arise from asymmetric fracture growth, as evidenced by the shape of the AE fronts.

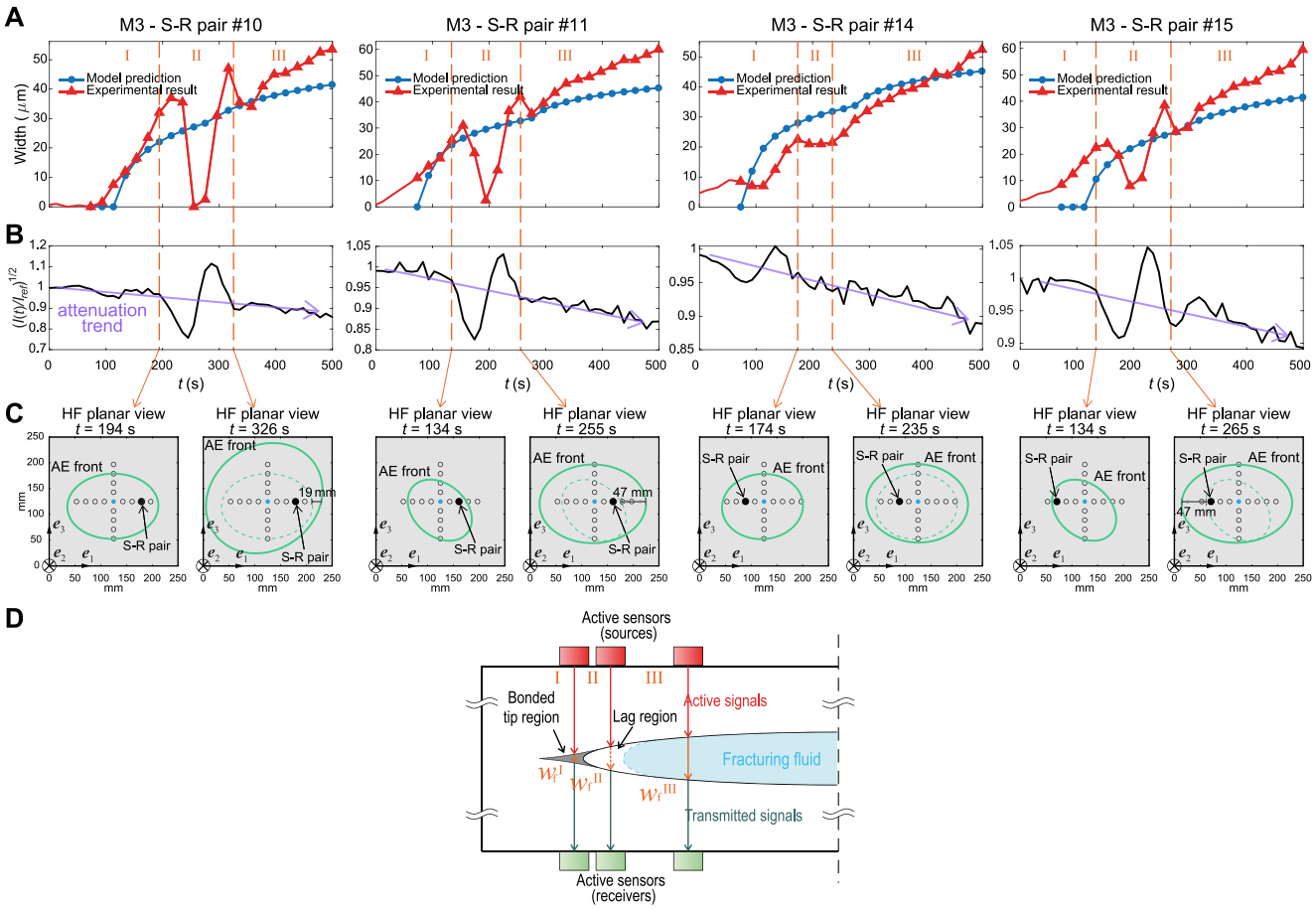

Figure 7. (a) Width evolution at source-receiver pairs #10, 11, 14, and 15 in experiment M3. (b) Attenuation of transmitted signals at all locations. (c) Snapshots of acoustic emission (AE) fronts at both the beginning and the end of phase II at the location of each source-receiver pair. The fluid lag is estimated by the horizontal distance (along $\boldsymbol{e}_1$) between the two AE fronts. (d) Conceptual sketch of the tip region undergoing three phases as fracture front crosses the compressional-wave pathway.

4. Discussion

Theoretically, the impact of rock anisotropy was found to vary between propagation regimes (Moukhtari et al., 2020). However, for a given regime, the fracture shape evolves in a self-similar manner and can be grasped by the aspect ratio between the major and minor semi-axes of the fracture footprint noted as a/b. Two relations have been proposed for a/b corresponding to HF propagation respectively in the toughness- and viscosity-dominated regimes (Moukhtari et al., 2020). The aspect ratio is the lowest in the viscosity-dominated regime, and is found to evolve as

$$a/b \approx \left[0.76\left(E_3'/E_1'\right)^{1/3} + 0.24\right]^{-1} \tag{5}$$

In the toughness-dominated regime, the elongation is more pronounced and the aspect ratio scales as

$$a/b = \left(\frac{K_{\mathrm{Ic},3} \cdot E_1'}{K_{\mathrm{Ic},1} \cdot E_3'}\right)^2 \tag{6}$$

Equation 6 provides the exact value of aspect ratio derived for an elliptical quasi-static fracture propagating under uniform loading (identical to the loading conditions in the toughness-dominate regime) in a transversely isotropic medium. Equation 5 is an approximation derived from self-similar viscosity-dominated HF footprints with

varying E'_3/E'_1 obtained in numerical simulations (Moukhtari et al., 2020). The two solutions indicate that the elastic stiffnesses anisotropy, E'_3/E'_1, always plays a role in the determination of the fracture shape regardless of the propagation regime. However, its influence in the viscosity-dominated regime, $(E'_1/E'_3)^{1/3}$, is significantly less than in the toughness-dominated regime, $(E'_1/E'_3)^2$. On the other hand, the degree of anisotropy in fracture toughness, $K_{Ic,3}/K_{Ic,1}$, holds a similar influence as the anisotropic elastic stiffnesses in the toughness-dominated regime. Nevertheless, it becomes irrelevant in the viscosity-dominated regime, where the majority of energy dissipates through the viscous fluid flow, instead of the creation of new fracture surfaces.

The values of a/b measured from lab experiments are compared to these two solutions, as well as the numerical predictions (Figures 2b and 2c). We find in K1 that a/b first rises above the toughness regime limit when the HF growth is partially stopped by the foliation plane. Its value then drops and converges to the toughness limit as the HF regains the elliptical shape as its center is shifted downward. The reconstructed AE front in T2 is seen to be less elliptical compared to the model predictions at the beginning as the AEs are more scattered, but it approaches the numerical predictions as the HF propagation continues.

Interestingly, we observe an unexpected elliptical front shape in both viscosity-dominated regime tests at the beginning of propagation, and a/b ultimately decreases to ~1 (approaching a circular footprint). Such initial uneven fracture growth is likely related to the fluid lag at the beginning of fracture growth. It has been established (Bunger & Detournay, 2007; D. Garagash, 2006; Lecampion & Detournay, 2007) that although the fluid lag may be large at early-time of the propagation, it ultimately coalesces with the fracture front over a characteristic time-scale of order $E'^3\mu'/\sigma^3_{h\min}$ (where $\sigma_{h\min}$ is the minimum confining stress). In the case of an initially significant fluid lag (with the order of magnitude of $O(10^1)$ mm as estimated in Section 3.3), the shape of the HF is primarily determined by the rock's anisotropic characteristics since the tip is dry and the viscous fluid is mainly contained in the initial notch, which is akin to applying a concentrated mechanical load at the centroid. This explains why an elliptical shape is observed at early time, while the fracture becomes ultimately more radial as the fluid reaches the fracture front. Hence, our findings have confirmed that the two solutions can effectively estimate the overall fracture shape in both limiting regimes, particularly during late stages of fracture propagation, when the initial dominance by fluid lag has vanished. It is worthwhile to note that in order for the limiting solutions 5 and 6 to be applicable, both the upper and lower bounds of $\mathcal{K}_m$ should be located within the corresponding regime (either the toughness-dominated or viscosity-dominated regime). This is confirmed by the scaling analysis detailed in Dontsov (2019).

The intrinsic anisotropy of the rock is also evident in the topography of the created fracture surfaces. The post-test photograph and the 3D roughness profile of part of the fracture plane created in M3 (Figures 8a and 8b), as well as the main principal surface curvature plots in Figure 8c show a clear direction-dependent rough surface characterized by parallel grooves aligned with the orientation of foliation planes. The importance of heterogeneity on controlling fracture roughness has been recently well quantified for a model material (hydrogel) (Steinhardt & Rubinstein, 2022). The anisotropic fracture roughness, with a rougher texture across the rock's internal layering and a smoother texture in the parallel-to-foliation direction, can thus be attributed to different length-scales of heterogeneity in the perpendicular and parallel-to-foliation directions associated with the rock deposition. Naturally, the propagation of fractures along the rougher direction necessitates higher energy consumption compared to the smoother direction, which is thereby speculated to be one factor that causes the elongation of these fractures.

5. Conclusions

Hydraulic fracturing experiments and numerical simulations are conducted to explore the impact of anisotropic elastic stiffnesses and fracture toughness on the planar fracture growth in a transversely isotropic rock across different propagation regimes. The experimental setup is designed to ensure that the fracture propagates normally to the material isotropy plane and to minimize the non-planar fracture growth. Clear correlation between the aspect ratio of a HF, a/b, and the dimensionless toughness, $\mathcal{K}_m$, is revealed by both experimental and simulation results (Figures 2a and 2b)—larger $\mathcal{K}_m$ results in a more elongated HF shape that restricts the fracture growth in the perpendicular-to-foliation orientation, whereas smaller $\mathcal{K}_m$ leads to a more isotropic propagation. We conclude that rock anisotropy has a dominating effect on the vertical containment/horizontal elongation of HFs in the absence of variation in confining stresses and material properties. We have clearly demonstrated that an intrinsic layering of rock formation, which is reflected in a transversely isotropic behavior at a larger scale, can favor the containment of HF at depth when the orientation of the material isotropy plane is perpendicular to the

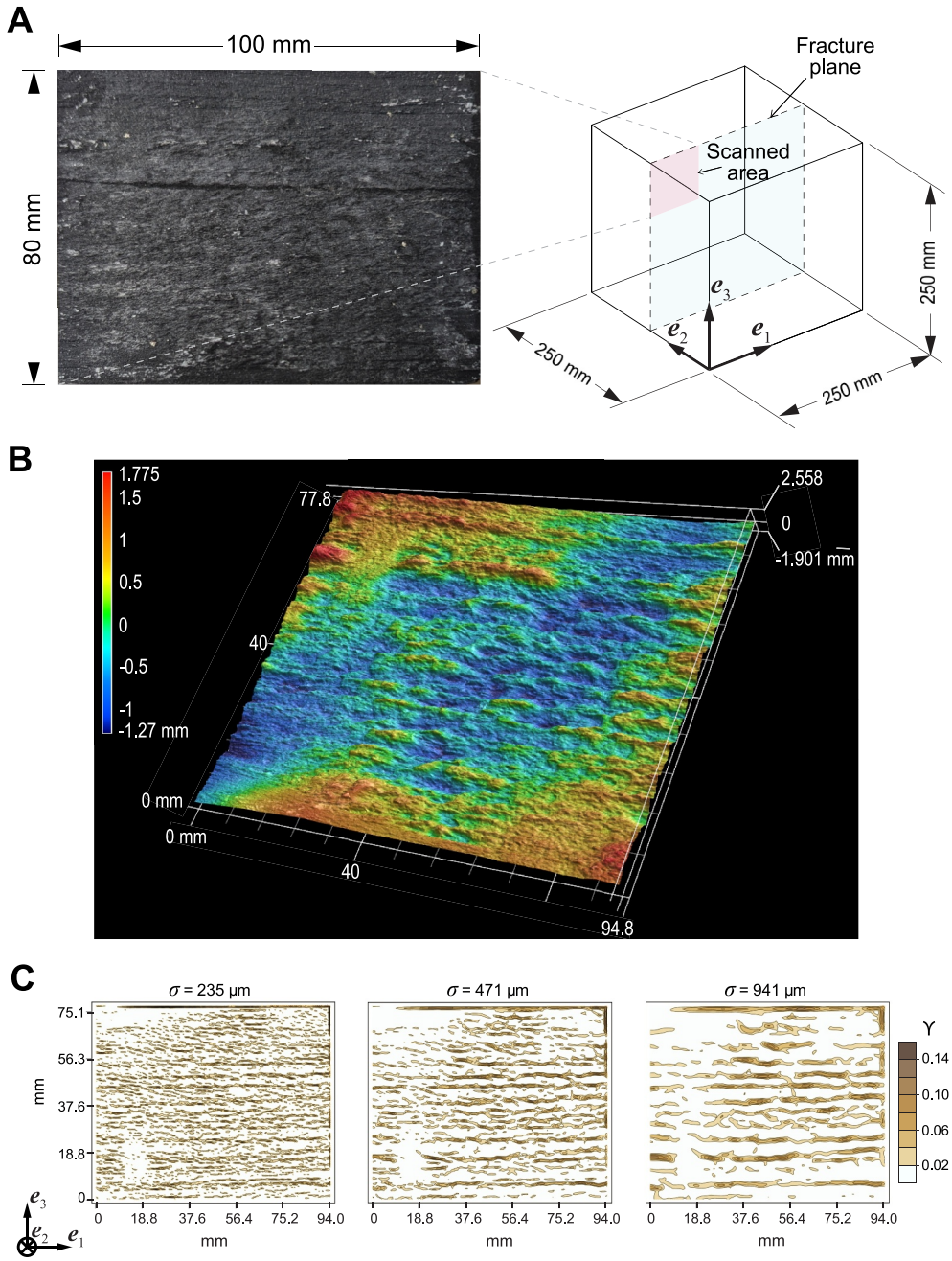

Figure 8. (a) Post-test photograph of the direction-dependent rough fracture surface of a part of the fracture plane created in M3 (80 mm × 100 mm). (b) 3D profile of the same partial fracture plane mapped by a Keyence VR-3200 optical profilometer with a voxel resolution of 47 μm^3. (c) An estimate for the main principal surface curvature Υ (see Appendix C) of the original surface elevation profile is plotted at three different scales (from left to right: $\sigma = 235$ μm, $\sigma = 471$ μm, $\sigma = 941$ μm). The repeated bands of stark contrast representing high curvature are oriented in the same direction as the inherent layering ($\boldsymbol{e}_1$) and coincide with parallel grooves recognizable by direct inspection of the fracture surface.

minimum confining stress. Such a configuration is ubiquitous in sedimentary basins worldwide. Including the effect of rock anisotropy more systematically—with proper material characterization—is clearly needed in order to reconcile field observations further. More importantly, our results highlight the fact that the injection parameters (larger fracturing fluid viscosity and larger injection rate) can suppress the beneficial impact of material anisotropy on fracture containment by increasing the energy spent in viscous fluid flow (see Equation 3). The

results presented here open the door to a more consistent engineering design of hydraulic fracturing treatments in shales with respect to their confinement at depth.

Appendix A: Transversely Isotropic Mechanical Properties of Slate

For a linear elastic transversely isotropic material, the stress-strain correlation in Voigt form is given by

$$\begin{pmatrix}\sigma_{11}\\ \sigma_{22}\\ \sigma_{33}\\ \sigma_{23}\\ \sigma_{13}\\ \sigma_{12}\end{pmatrix}=\begin{bmatrix} C_{11} & (C_{11}-2C_{66}) & C_{13} & 0 & 0 & 0\\ (C_{11}-2C_{66}) & C_{22} & C_{13} & 0 & 0 & 0\\ C_{13} & C_{13} & C_{33} & 0 & 0 & 0\\ 0 & 0 & 0 & C_{44} & 0 & 0\\ 0 & 0 & 0 & 0 & C_{44} & 0\\ 0 & 0 & 0 & 0 & 0 & C_{66}\end{bmatrix}\begin{pmatrix}\epsilon_{11}\\ \epsilon_{22}\\ \epsilon_{33}\\ 2\epsilon_{23}\\ 2\epsilon_{13}\\ 2\epsilon_{12}\end{pmatrix} \tag{A1}$$

in which $\boldsymbol{\sigma}$ and $\boldsymbol{\epsilon}$ are the stress and strain tensors, and C_{ij} denotes the five independent (11, 22, 33, 13, 44, 66) elastic stiffnesses of a transversely isotropic material (with indices i and j defined by the material coordinate system in Figure 1a). The linear elastic constitutive relation A1 can be expressed in terms of the compliance tensor using the engineering elastic parameters (E_1, E_3, ν_{12}, ν_{13}, G_{13}):

$$\begin{pmatrix}\epsilon_{11}\\ \epsilon_{22}\\ \epsilon_{33}\\ 2\epsilon_{23}\\ 2\epsilon_{13}\\ 2\epsilon_{12}\end{pmatrix}=\begin{bmatrix} 1/E_1 & -\nu_{12}/E_1 & -\nu_{13}/E_3 & 0 & 0 & 0\\ -\nu_{12}/E_1 & 1/E_1 & -\nu_{12}/E_1 & 0 & 0 & 0\\ -\nu_{13}/E_3 & -\nu_{12}/E_1 & 1/E_3 & 0 & 0 & 0\\ 0 & 0 & 0 & 1/G_{13} & 0 & 0\\ 0 & 0 & 0 & 0 & 1/G_{13} & 0\\ 0 & 0 & 0 & 0 & 0 & 2(1+\nu_{12})/E_1\end{bmatrix}\begin{pmatrix}\sigma_{11}\\ \sigma_{22}\\ \sigma_{33}\\ \sigma_{23}\\ \sigma_{13}\\ \sigma_{12}\end{pmatrix} \tag{A2}$$

Accordingly, the components in the compliance tensor in Equation A2 can be obtained by inverting the stiffness tensor **C**. Their values are determined by the ultrasonic wave-speeds measured along different directions with respect to the plane of isotropy (Tsvankin, 2012; Wang, 2002a) and are given in Table A1. In addition, we report the values of following Thomsen parameters (Thomsen, 1986):

$$\begin{aligned}\epsilon &= \frac{C_{11}-C_{33}}{2C_{33}}\\ \gamma &= \frac{C_{66}-C_{44}}{2C_{44}}\\ \delta &= \frac{(C_{13}+C_{44})^2-(C_{33}-C_{44})^2}{2C_{33}(C_{33}-C_{44})}\end{aligned} \tag{A3}$$

Table A1
Transversely Isotropic Elastic Stiffnesses, Engineering Elastic Parameters, Thomsen Parameters, and Fracture Toughness of the Del Carmen Slate Rock

Elastic stiffnesses C_{ij} (GPa)	Engineering parameters	Plane-strain elastic modulus (GPa)	Thomsen parameters	Fracture toughness (MPa$\sqrt{m}$)
C_{11} = 114.6	E_1 = 107.4 (GPa)	E_1 = 107.5	ϵ = 0.26	$K_{Ic,1}$ = 2.5
C_{13} = 4.7	E_3 = 75.2 (GPa)	E_3 = 97.2	γ = 0.1	$K_{Ic,3}$ = 3.5
C_{33} = 75.5	G_{13} = 35.9 (GPa)		δ = 0.013	
C_{44} = 35.9	ν_{12} = 0.246			
C_{66} = 43.1	ν_{13} = 0.033			

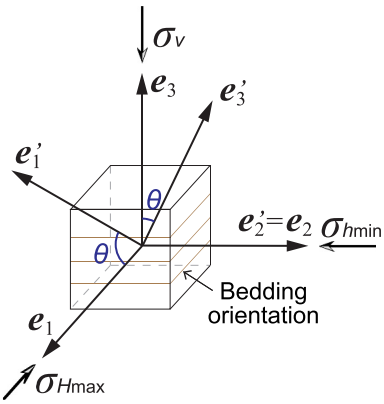

Figure A1. Schematic sketch of 3-D transformation between the global ($\boldsymbol{e}_1$, $\boldsymbol{e}_2$, $\boldsymbol{e}_3$) and the local coordinate system $(\boldsymbol{e}_1',\boldsymbol{e}_2',\boldsymbol{e}_3')$. The local fracture front propagates along the $\boldsymbol{e}_1$ direction.

The elastic stiffnesses appear to be highly consistent among all samples, as the standard deviations of the ultrasonic wave-speeds are, on average, less than 1% of the mean values (e.g., $V_P(\theta = 0) = 6{,}432 \pm 41$ m/s). Additionally, the variation of confining stresses have limited effect on the measured wave-speeds. The values of wave-speeds used in this work are measured under actual confining stresses in the experiments. The values of two fracture toughnesses, $K_{\mathrm{Ic},1}$ and $K_{\mathrm{Ic},3}$, are also given in Table A1.

To obtain the local (at crack tip) elastic modulus (E') and fracture toughness (K_{Ic}) with orientation θ, the elastic stiffness tensor, $\mathbf{C}$, needs to be rotated from the global to the local coordinate system (Figure A1). This can be achieved by applying a transformation matrix $\mathbf{T}$:

$$\mathbf{C}' = \mathbf{TCT}' \tag{A4}$$

and $\mathbf{T}$ is computed as

$$\mathbf{T} = \begin{bmatrix} l_1^2 & m_1^2 & n_1^2 & 2m_1n_1 & 2l_1n_1 & 2l_1m_1 \\ l_2^2 & m_2^2 & n_2^2 & 2m_2n_2 & 2l_2n_2 & 2l_2m_2 \\ l_3^2 & m_3^2 & n_3^2 & 2m_3n_3 & 2l_3n_3 & 2l_3m_3 \\ l_2l_3 & m_2m_3 & n_2n_3 & m_2n_3+m_3n_2 & l_2n_3+l_3n_2 & l_2m_3+l_3m_2 \\ l_1l_3 & m_1m_3 & n_1n_3 & m_1n_3+m_3n_1 & l_1n_3+l_3n_1 & l_1m_3+l_3m_1 \\ l_1l_2 & m_1m_2 & n_1n_2 & m_1n_2+m_2n_1 & l_1n_2+l_2n_1 & l_1m_2+l_2m_1 \end{bmatrix}$$

where l_i, m_i, n_i ($i = 1, 2, 3$) are the direction cosines between the major axes before and after rotation (for instance, $l_1 = \cos(\boldsymbol{e}_1',\boldsymbol{e}_1) = \cos\theta$ and $m_1 = \cos(\boldsymbol{e}_1',\boldsymbol{e}_2) = 0$). Using Equation A4, the values of C_{ij}' can be calculated.

Appendix B: Passive and Active Acoustic Methods

Examples of AE waveforms in test K1 are provided in Figure B1. The 3D localization algorithm takes into account the transverse isotropy of slate by using the value of directional dependent compressional-wave velocity (Thomsen, 1986). For the weakly anisotropic slate, the phase velocity introduced in Thomsen (1986) is used. To track the advancement of the micro-cracking frontier, we first pick the outermost events (one event from every 10° angular sector) detected in a fixed time interval prior to the time of interest (150 s time window in the example of T2, shown in Figure B1C). Next, an ellipse-specific fitting method (Bookstein, 1979; Fitzgibbon et al., 1999) is applied to reconstruct the elliptical AE front as recovered in Figure B1C.

In active wave transmission analysis, w_{f} is solved by minimizing the difference between the transmitted signal in the frequency domain, $\hat{S}(\omega)$, and its theoretical value with width w_{f} (Groenenboom & Fokkema, 1998):

$$\hat{S}^T(\omega, w_{\mathrm{f}}) = \hat{T}(\omega, w_{\mathrm{f}})\,\hat{S}(\omega, 0) \tag{B1}$$

where the transmission coefficient, $\hat{T}(\omega, w_{\mathrm{f}})$, is computed by

$$\hat{T}(\omega, w_{\mathrm{f}}) = \frac{(1 - r_{ff}^2)\exp(-j\alpha)}{1 - r_{ff}^2\exp(-2j\alpha)}$$

with $r_{ff} = \frac{\rho_f v_{P,f} - \rho_s v_{P,s}}{\rho_f v_{P,f} + \rho_s v_{P,s}}$ and $\alpha = \frac{\omega w_{\mathrm{f}}}{v_{P,f}}$. ρ_s and ρ_f denote the density of the solid and fluid, respectively. $v_{P,s}$ and $v_{P,f}$ are the compressional-wave velocities in the solid and fluid. These values are measured prior to experiments and are reported as: $\rho_s = 2{,}770$ kg/m^3, $\rho_f = 1{,}560$ kg/m^3 (glucose), $\rho_f = 1{,}260$ kg/m^3 (glycerol), $v_{P,s} = 6{,}432$ m/s, $v_{P,s} = 2{,}000$ m/s (glucose), $v_{P,s} = 2{,}000$ m/s (glycerol).

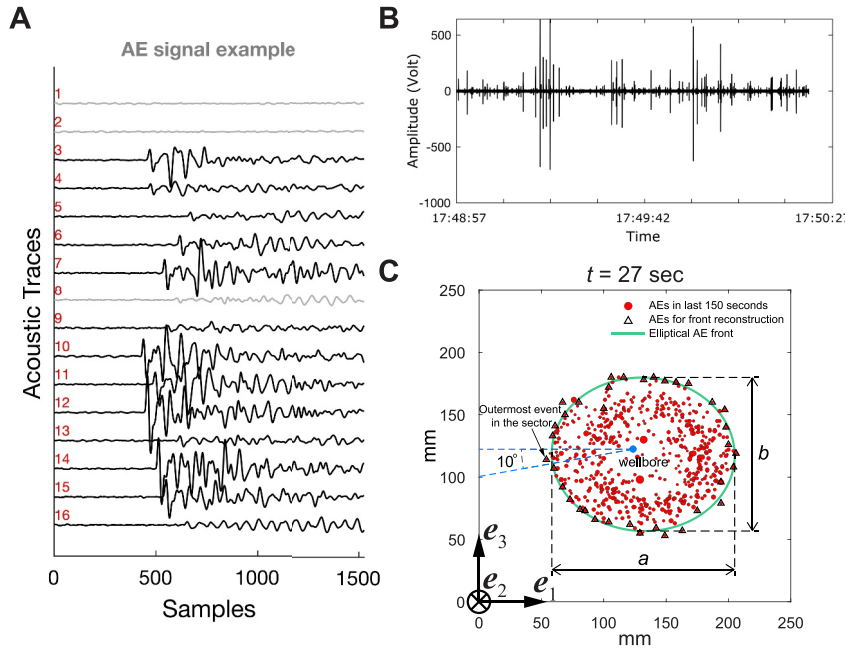

Figure B1. (a) Example acoustic emission (AE) signals in an event in test K1. The signal has a sampling rate of 10 MHz. Sensor numbers are in red. Signals with low signal-to-noise ratio are plotted in Gray. (b) An example of acoustic signal belonging to sensor #6 throughout the lifetime of K1. AEs are visible. (c) Illustration of the elliptical AE front reconstruction in test T2 (t = 27 s).

Appendix C: Fracture Surface Roughness Measurement

The 3D surface elevation profile of part of the fracture plane created in M3 (see Figure 8) has been measured using an optical profilometer (VR-3200, Keyence Corporation). For the scanned 80 mm × 100 mm surface, a voxel resolution of 47 μm^3 is used. To highlight the strong anisotropy of the surface, a second-order Gaussian derivative filter has been applied at different scales σ to estimate the local Hessian matrix. The main negative eigenvalue of the Hessian matrix which corresponds to the main principal curvature orthogonal to a ridge is then plotted in Figure 4 (see Mathematica © RidgeFilter command for details).

Conflict of Interest

The authors declare no conflicts of interest relevant to this study.

Data Availability Statement

The raw active acoustic data, as well as the processed experimental data, including the fluid injection records and detailed acoustic emission results are available on Zenodo (https://doi.org/10.5281/zenodo.7738236) (Lu, Momeni, Perruzo, et al., 2022). We also provide processed experimental data as source data for the figures used in this paper. The raw passive acoustic dataset for the 16 channels recorded in continuous mode is too large (several TBs) to share in a public repository but can be made available upon request. The hydraulic fracture simulator Pyfrac (Zia & Lecampion, 2020; Zia et al., 2024) is available at https://github.com/GeoEnergyLab-EPFL/PyFrac (https://doi.org/10.5281/zenodo.10794247). The source code for fracture width estimation from the active acoustic measurement (Blum & Lecampion, 2024) is available at https://github.com/GeoEnergyLab-EPFL/FracMonitoring.git (https://doi.org/10.5281/zenodo.10807757).

Acknowledgments
This work was funded by the Swiss National Science Foundation through Grants 160577 and no. 192237. We are grateful to Prof. Pedro M. Reis for generously providing access to the surface roughness measurement equipment. We thank Dr. T. Adatte for the X-ray powder diffraction measurement of the Del Carmen slate mineralogy. Open access funding provided by Ecole Polytechnique Federale de Lausanne.

References

Abbas, S., & Lecampion, B. (2013). Initiation and breakdown of an axisymmetric hydraulic fracture transverse to a horizontal wellbore. In A. P. Bunger, J. McLennan, & R. G. Jeffrey (Eds.), *Effective and sustainable hydraulic fracturing (chapter 19)*. Intech.

Benouadah, N., Dontsov, E., Badrouchi, F., & Rasouli, V. (2023). Impact of toughness anisotropy on fracture initiation pressure and morphology in shale rocks. *Rock Mechanics and Rock Engineering*, *56*(12), 9149–9168. https://doi.org/10.1007/s00603-023-03502-0

Bessmertnykh, A., & Dontsov, E. (2018). Aspect ratio of hydraulic fracture in homogeneous transversely isotropic material. In *Proceedings 52nd US rock mechanics/geomechanics symposium. (ARMA 18-268)*.

Blum, T., & Lecampion, B. (2024). GeoEnergyLab-EPFL/Fracmonitoring: Version 0.1.1 [Software]. *Zenodo*. https://doi.org/10.5281/zenodo.10807757

Bookstein, F. L. (1979). Fitting conic sections to scattered data. *Computer Graphics and Image Processing*, *9*(1), 56–71. https://doi.org/10.1016/0146-664X(79)90082-0

Bunger, A. P., & Detournay, E. (2007). Early-time solution for a radial hydraulic fracture. *ASCE Journal of Engineering Mechanics*, *133*(5), 534–540. https://doi.org/10.1061/(asce)0733-9399(2007)133:5(534)

Bunger, A. P., & Detournay, E. (2008). Experimental validation of the tip asymptotics for a fluid-driven fracture. *Journal of the Mechanics and Physics of Solids*, *56*(11), 3101–3115. https://doi.org/10.1016/j.jmps.2008.08.006

Bunger, A. P., & Lecampion, B. (2017). Four critical issues for successful hydraulic fracturing applications. In X.-T. Feng (Ed.), *Rock mechanics and engineering* (1st ed., Vol. 5, pp. 551–593). CRC Press/Balkema.

Chandler, M., Meredith, P., Brantut, N., & Crawford, B. (2016). Fracture toughness anisotropy in shale. *Journal of Geophysical Research: Solid Earth*, *121*(3), 1706–1729. https://doi.org/10.1002/2015JB012756

Chang, S.-H., & Lee, C.-I. (2004). Estimation of cracking and damage mechanisms in rock under triaxial compression by moment tensor analysis of acoustic emission. *International Journal of Rock Mechanics and Mining Sciences*, *41*(7), 1069–1086. https://doi.org/10.1016/j.ijrmms.2004.04.006

Chertov, M. (2012). Closed-form solution for vertical fracture width in anisotropic elastic formations. *International Journal of Rock Mechanics and Mining Sciences*, *53*, 70–75. https://doi.org/10.1016/j.ijrmms.2012.04.006

Cho, J.-W., Kim, H., Jeon, S., & Min, K.-B. (2012). Deformation and strength anisotropy of asan gneiss, boryeong shale, and yeoncheon schist. *International Journal of Rock Mechanics and Mining Sciences*, *50*, 158–169. https://doi.org/10.1016/j.ijrmms.2011.12.004

Ciezobka, J., Courtier, J., & Wicker, J. (2018). Hydraulic fracturing test site (hfts)-project overview and summary of results. In *SPE/AAPG/SEG unconventional resources technology conference*.

Detournay, E. (2004). Propagation regimes of fluid-driven fractures in impermeable rocks. *International Journal of Geomechanics*, *4*(1), 1–11. https://doi.org/10.1061/(asce)1532-3641(2004)4:1(35)

Detournay, E. (2016). Mechanics of hydraulic fractures. *Annual Review of Fluid Mechanics*, *48*(1), 311–339. https://doi.org/10.1146/annurev-fluid-010814-014736

Dontsov, E. V. (2019). Scaling laws for hydraulic fractures driven by a power-law fluid in homogeneous anisotropic rocks. *International Journal for Numerical and Analytical Methods in Geomechanics*, *43*(2), 519–529. https://doi.org/10.1002/nag.2874

Economides, M. & Nolte, K. (Eds.) (2000)., *Reservoir stimulation* (3rd ed.). John Wiley & Sons.

EPA. (2016). *Hydraulic fracturing for oil and gas: Impacts from the hydraulic fracturing water cycle on drinking water resources in the United States (technical report)*. Environmental Protection Agency.

Fisher, K., & Warpinski, N. (2012). Hydraulic fracture height growth: Real data. *SPE Production & Operations*, *27*(1), 8–19. https://doi.org/10.2118/145949-pa

Fitzgibbon, A., Pilu, M., & Fisher, R. (1999). Direct least square fitting of ellipses. *IEEE Transactions on Pattern Analysis and Machine Intelligence*, *21*(5), 476–480. https://doi.org/10.1109/34.765658

Flewelling, S. A., Tymchak, M. P., & Warpinski, N. (2013). Hydraulic fracture height limits and fault interactions in tight oil and gas formations. *Geophysical Research Letters*, *40*(14), 3602–3606. https://doi.org/10.1002/grl.50707

Fu, P., Settgast, R. R., Hao, Y., Morris, J. P., & Ryerson, F. J. (2017). The influence of hydraulic fracturing on carbon storage performance. *Journal of Geophysical Research: Solid Earth*, *122*(12), 9931–9949. https://doi.org/10.1002/2017JB014942

Garagash, D. (2006). Propagation of plane-strain hydraulic fracture with a fluid lag: Early-time solution. *International Journal of Solids and Structures*, *43*(18–19), 5811–5835. https://doi.org/10.1016/j.ijsolstr.2005.10.009

Garagash, D., & Detournay, E. (2000). The tip region of a fluid-driven fracture in an elastic medium. *ASME Journal of Applied Mechanics*, *67*(1), 183–192. https://doi.org/10.1115/1.321162

Garagash, D. I. (2009). Scaling of physical processes in fluid-driven fracture: Perspective from the tip. In F. Borodich (Ed.), *Iutam symposium on scaling in solid mechanics* (Vol. 10, pp. 91–100). Springer.

Gehne, S., Benson, P. M., Koor, N., Dobson, K. J., Enfield, M., & Barber, A. (2019). Seismo-mechanical response of anisotropic rocks under hydraulic fracture conditions: New experimental insights. *Journal of Geophysical Research: Solid Earth*, *124*(9), 9562–9579. https://doi.org/10.1029/2019JB017342

Gehne, S., Forbes Inskip, N. D., Benson, P. M., Meredith, P. G., & Koor, N. (2020). Fluid-driven tensile fracture and fracture toughness in nash point shale at elevated pressure. *Journal of Geophysical Research: Solid Earth*, *125*(2), e2019JB018971. https://doi.org/10.1029/2019JB018971

Groenenboom, J., & Fokkema, J. T. (1998). Monitoring the width of hydraulic fractures with acoustic waves. *Geophysics*, *63*(1), 139–148. https://doi.org/10.1190/1.1444306

Hampton, J., Gutierrez, M., & Matzar, L. (2019). Microcrack damage observations near coalesced fractures using acoustic emission. *Rock Mechanics and Rock Engineering*, *52*(10), 3597–3608. https://doi.org/10.1007/s00603-019-01818-4

Hampton, J., Gutierrez, M., Matzar, L., Hu, D., & Frash, L. (2018). Acoustic emission characterization of microcracking in laboratory-scale hydraulic fracturing tests. *Journal of Rock Mechanics and Geotechnical Engineering*, *10*(5), 805–817. https://doi.org/10.1016/j.jrmge.2018.03.007

Heng, S., Guo, Y., Yang, C., Daemen, J. J., & Li, Z. (2015). Experimental and theoretical study of the anisotropic properties of shale. *International Journal of Rock Mechanics and Mining Sciences*, *74*, 58–68. https://doi.org/10.1016/j.ijrmms.2015.01.003

Hirth, J. P., & Lothe, J. (1982). *Theory of dislocations*. John Wiley & Sons.

Hornby, B. E., Schwartz, L. M., & Hudson, J. A. (1994). Anisotropic effective?medium modeling of the elastic properties of shales. *Geophysics*, *59*(10), 1570–1583. https://doi.org/10.1190/1.1443546

Howarth, R., & Ingraffea, A. (2011). Natural gas: Should fracking stop? *Nature*, *477*(7364), 271–273. https://doi.org/10.1038/477271a

Hubbert, M., & Willis, D. (1957). Mechanics of hydraulic fracturing. *Trans. AIME*, *210*(01), 153–168. https://doi.org/10.2118/686-g

Jeffrey, R., & Bunger, A. P. (2009). A detailed comparison of experimental and numerical data on hydraulic fracture height growth through stress contrasts. *Society of Petroleum Engineers Journal*, *14*(3), 413–422. https://doi.org/10.2118/106030-pa

Johnston, J. E., & Christensen, N. I. (1995). Seismic anisotropy of shales. *Journal of Geophysical Research: Solid Earth*, *100*(B4), 5991–6003. https://doi.org/10.1029/95JB00031

Jones, L. E. A., & Wang, H. F. (1981). Ultrasonic velocities in cretaceous shales from the Williston basin. *Geophysics*, *46*(3), 288–297. https://doi.org/10.1190/1.1441199

Kohli, A., & Zoback, M. (2021). Stratigraphically controlled stress variations at the hydraulic fracture test site-1 in the midland basin, tx. *Energies*, *14*(24), 8328. https://doi.org/10.3390/en14248328

Kovalyshen, Y., Bunger, A. P., Kear, J., & Kasperczyk, D. (2014). Comparison between ultrasonic and photometric methods for hydraulic fracture laboratory monitoring. *International Journal of Rock Mechanics and Mining Sciences*, *70*, 368–374. https://doi.org/10.1016/j.ijrmms.2014.05.008

Kundu, T. (2014). Acoustic source localization. *Ultrasonics*, *54*(1), 25–38. https://doi.org/10.1016/j.ultras.2013.06.009

Kuruppu, M., Obara, Y., Ayatollahi, M., Chong, K., & Funatsu, T. (2014). Isrm-suggested method for determining the mode i static fracture toughness using semi-circular bend specimen. *Rock Mechanics and Rock Engineering*, *47*(1), 267–274. https://doi.org/10.1007/s00603-013-0422-7

Laubie, H., & Ulm, F.-J. (2014). Irwin?s conjecture: Crack shape adaptability in transversely isotropic solids. *Journal of the Mechanics and Physics of Solids*, *68*, 1–13. https://doi.org/10.1016/j.jmps.2014.03.004

Lecampion, B., Desroches, J., Jeffrey, R. G., & Bunger, A. P. (2017). Experiments versus theory for the initiation and propagation of radial hydraulic fractures in low-permeability materials. *Journal of Geophysical Research: Solid Earth*, *122*(2), 1239–1263. https://doi.org/10.1002/2016jb013183

Lecampion, B., & Detournay, E. (2007). An implicit algorithm for the propagation of a plane strain hydraulic fracture with fluid lag. *Computer Methods in Applied Mechanics and Engineering*, *196*(49–52), 4863–4880. https://doi.org/10.1016/j.cma.2007.06.011

Liu, D., & Lecampion, B. (2022a). Laboratory investigation of hydraulic fracture growth in Zimbabwe gabbro. *Journal of Geophysical Research: Solid Earth*, *127*(11), e2022JB025678. https://doi.org/10.1029/2022JB025678

Liu, D., & Lecampion, B. (2022b). Measurements of the evolution of the fluid lag in laboratory hydraulic fracture experiments in rocks. In X. Zhang, B. Wu, & A. Bunger (Eds.), *Mechanics of hydraulic fracturing: Experiment, model and monitoring* (pp. 11–25). John Wiley & Sons.

Liu, D., Lecampion, B., & Blum, T. (2020). Time-lapse reconstruction of the fracture front from diffracted waves arrivals in laboratory hydraulic fracture experiments. *Geophysical Journal International*, *223*(1), 180–196. https://doi.org/10.1093/gji/ggaa310

Lockner, D. (1993). The role of acoustic emission in the study of rock fracture. *International Journal of Rock Mechanics and Mining Sciences*, *30*(7), 883–899. https://doi.org/10.1016/0148-9062(93)90041-b

Lu, G., Crandall, D., & Bunger, A. P. (2021). Observations of breakage for transversely isotropic shale using acoustic emission and x-ray computed tomography: Effect of bedding orientation, pre-existing weaknesses, and pore water. *International Journal of Rock Mechanics and Mining Sciences*, *139*, 104650. https://doi.org/10.1016/j.ijrmms.2021.104650

Lu, G., Gordeliy, E., Prioul, R., & Bunger, A. P. (2017). Modeling initiation and propagation of a hydraulic fracture under subcritical conditions. *Computer Methods in Applied Mechanics and Engineering*, *318*, 61–91. https://doi.org/10.1016/j.cma.2017.01.018

Lu, G., Momeni, S., & Lecampion, B. (2022). Experimental investigation of hydraulic fracture growth in an anisotropic rock with pre-existing discontinuities under different propagation regimes. In *Proceedings 56th us rock mechanics/geomechanics symposium. (ARMA 22-239)*.

Lu, G., Momeni, S., Perruzo, C., Moukhtari, F.-E., & Lecampion, B. (2022). Rock anisotropy promotes hydraulic fracture containment at depth. [Dataset]. https://doi.org/10.5281/zenodo.7738235

Meléndez-Martínez, J., & Schmitt, D. R. (2016). A comparative study of the anisotropic dynamic and static elastic moduli of unconventional reservoir shales: Implication for geomechanical investigations. *Geophysics*, *81*(3), D245–D261. https://doi.org/10.1190/geo2015-0427.1

Momeni, S., Liu, D., & Lecampion, B. (2021). Combining active and passive acoustic methods to image hydraulic fracture growth in laboratory experiments. *IOP Conference Series: Earth and Environmental Science*, *833*(1), 1–9. https://doi.org/10.1088/1755-1315/833/1/012088

Moukhtari, F.-E. (2020). *Propagation of fluid driven fractures in transversely isotropic material (Unpublished doctoral dissertation)*. École polytechnique fédérale de Lausanne (EPFL).

Moukhtari, F.-E., Lecampion, B., & Zia, H. (2020). Planar hydraulic fracture growth perpendicular to the isotropy plane in a transversely isotropic material. *Journal of the Mechanics and Physics of Solids*, *137*, 103878. https://doi.org/10.1016/j.jmps.2020.103878

Nasseri, M., Grasselli, G., & Mohanty, B. (2010). Fracture toughness and fracture roughness in anisotropic granitic rocks. *Rock Mechanics and Rock Engineering*, *43*(4), 403–415. https://doi.org/10.1007/s00603-009-0071-z

Ong, O. N., Schmitt, D. R., Kofman, R. S., & Haug, K. (2016). Static and dynamic pressure sensitivity anisotropy of a calcareous shale. *Geophysical Prospecting*, *64*(4), 875–897. https://doi.org/10.1111/1365-2478.12403

Osborn, S. G., Vengosh, A., Warner, N. R., & Jackson, R. B. (2011). Methane contamination of drinking water accompanying gas-well drilling and hydraulic fracturing. *Proceedings of the National Academy of Sciences of the United States of America*, *108*(20), 8172–8176. https://doi.org/10.1073/pnas.1100682108

Savitski, A., & Detournay, E. (2002). Propagation of a penny-shaped fluid-driven fracture in an impermeable rock: Asymptotic solutions. *International Journal of Solids and Structures*, *39*(26), 6311–6337. https://doi.org/10.1016/s0020-7683(02)00492-4

Schrag, D. P. (2007). Preparing to capture carbon. *Science*, *315*(5813), 812–813. https://doi.org/10.1126/science.1137632

Sesetty, V., & Ghassemi, A. (2018). Effect of rock anisotropy on wellbore stresses and hydraulic fracture propagation. *International Journal of Rock Mechanics and Mining Sciences*, *112*, 369–384. https://doi.org/10.1016/j.ijrmms.2018.09.005

Shah, K. R., & Labuz, J. F. (1995). Damage mechanisms in stressed rock from acoustic emission. *Journal of Geophysical Research: Solid Earth*, *100*(B8), 15527–15539. https://doi.org/10.1029/95JB01236

Simonson, E. R., Abou-Sayed, A. S., & Clifton, R. J. (1978). Containment of massive hydraulic fractures. *SPE Journal*, *18*(1), 27–32. https://doi.org/10.2118/6089-pa

Smith, M., & Montgomery, C. (2015). *Hydraulic fracturing* (1st ed.). CRC Press.

Sone, H., & Zoback, M. D. (2013). Mechanical properties of shale-gas reservoir rocks — Part 1: Static and dynamic elastic properties and anisotropy. *Geophysics*, *78*(5), D381–D392. https://doi.org/10.1190/geo2013-0050.1

Steinhardt, W., & Rubinstein, S. M. (2022). How material heterogeneity creates rough fractures. *Physical Review Letters*, *129*(12), 128001. https://doi.org/10.1103/PhysRevLett.129.128001

Tan, P., Jin, Y., Han, K., Hou, B., Chen, M., Guo, X., & Gao, J. (2017). Analysis of hydraulic fracture initiation and vertical propagation behavior in laminated shale formation. *Fuel*, *206*, 482–493. https://doi.org/10.1016/j.fuel.2017.05.033

Teufel, L. W., & Clark, J. A. (1984). Hydraulic fracture propagation in layered rock: Experimental studies of fracture containment. *SPE Journal*, *24*(1), 19–32. https://doi.org/10.2118/9878-pa

Thomsen, L. (1986). Weak elastic anisotropy. *Geophysics*, *51*(10), 1954–1966. https://doi.org/10.1190/1.1442051

Tsvankin, I. (2012). *Seismic signatures and analysis of reflection data in anisotropic media*. Society of Exploration Geophysicists.

van Eekelen, H. (1982). Hydraulic fracture geometry: Fracture containment in layered formation. *Society of Petroleum Engineers Journal*, *22*(3), 341–349. https://doi.org/10.2118/9261-pa

Vengosh, A., Jackson, R. B., Warner, N., Darrah, T. H., & Kondash, A. (2014). A critical review of the risks to water resources from unconventional shale gas development and hydraulic fracturing in the United States. *Environmental Science & Technology*, *48*(15), 8334–8348. https://doi.org/10.1021/es405118y

Vidic, R. D., Brantley, S. L., Vandenbossche, J. M., Yoxtheimer, D., & Abad, J. D. (2013). Impact of shale gas development on regional water quality. *Science*, *340*(6134), 1235009. https://doi.org/10.1126/science.1235009

Wang, Z. (2002a). Seismic anisotropy in sedimentary rocks, part 1: A single-plug laboratory method. *Geophysics*, *67*(5), 1415–1422. https://doi.org/10.1190/1.1512787

Wang, Z. (2002b). Seismic anisotropy in sedimentary rocks, part 2: Laboratory data. *Geophysics*, *67*(5), 1423–1440. https://doi.org/10.1190/1.1512743

Warner, N., Jackson, R., Darrah, T., Osborn, S., Down, A., Zhao, K., et al. (2012). Geochemical evidence for possible natural migration of marcellus formation brine to shallow aquifers in Pennsylvania. *Proceedings of the National Academy of Sciences of the United States of America*, *109*(30), 11961–11966. https://doi.org/10.1073/pnas.1121181109

Warpinski, N., Schmidt, R., & Northrop, D. (1982). In-situ stresses: The predominant influence of hydraulic fracture containment. *Journal of Petroleum Technology*, *34*(3), 653–664. https://doi.org/10.2118/8932-pa

Warpinski, N. R., & Teufel, L. W. (1987). Influence of geologic discontinuities on hydraulic fracture propagation. *Society of Petroleum Engineers Journal*, *39*(2), 209–220. https://doi.org/10.2118/13224-pa

Wong, R. C. K., Schmitt, D. R., Collis, D., & Gautam, R. (2008). Inherent transversely isotropic elastic parameters of over-consolidated shale measured by ultrasonic waves and their comparison with static and acoustic in situ log measurements. *Journal of Geophysics and Engineering*, *5*(1), 103–117. https://doi.org/10.1088/1742-2132/5/1/011

Xing, P., Yoshioka, K., Adachi, J., El-Fayoumi, A., & Bunger, A. P. (2018). 02). Laboratory demonstration of hydraulic fracture height growth across weak discontinuities. *Geophysics*, *83*(2), MR93–MR105. https://doi.org/10.1190/geo2016-0713.1

Zang, A., Christian Wagner, F., Stanchits, S., Dresen, G., Andresen, R., & Haidekker, M. A. (1998). Source analysis of acoustic emissions in Aue granite cores under symmetric and asymmetric compressive loads. *Geophysical Journal International*, *135*(3), 1113–1130. https://doi.org/10.1046/j.1365-246X.1998.00706.x

Zhang, S., Shou, K., Xian, X., Zhou, J., & Liu, G. (2018). Fractal characteristics and acoustic emission of anisotropic shale in brazilian tests. *Tunnelling and Underground Space Technology*, *71*, 298–308. https://doi.org/10.1016/j.tust.2017.08.031

Zhang, X., Jeffrey, R. G., & Thiercelin, M. (2007). Deflection and propagation of fluid-driven fractures at frictional bedding interfaces: A numerical investigation. *Journal of Structural Geology*, *29*(3), 396–410. https://doi.org/10.1016/j.jsg.2006.09.013

Zhang, Y., Long, A., Zhao, Y., Zang, A., & Wang, C. (2023). Mutual impact of true triaxial stress, borehole orientation and bedding inclination on laboratory hydraulic fracturing of lushan shale. *Journal of Rock Mechanics and Geotechnical Engineering*, *15*(12), 3131–3147. https://doi.org/10.1016/j.jrmge.2023.02.015

Zhao, H., Liang, B., Sun, W., Hu, Z., Ma, Y., & Liu, Q. (2022). Effects of hydrostatic pressure on hydraulic fracturing properties of shale using x-ray computed tomography and acoustic emission. *Journal of Petroleum Science and Engineering*, *215*, 110725. https://doi.org/10.1016/j.petrol.2022.110725

Zhou, J., Chen, M., Jin, Y., & Zhang, G. (2008). Analysis of fracture propagation behavior and fracture geometry using a tri-axial fracturing system in naturally fractured reservoirs. *International Journal of Rock Mechanics and Mining Sciences*, *45*(7), 1143–1152. https://doi.org/10.1016/j.ijrmms.2008.01.001

Zhou, Q., Xie, H., Zhu, Z., He, R., Lu, H., Fan, Z., et al. (2023). Fracture toughness anisotropy in shale under deep in situ stress conditions. *Rock Mechanics and Rock Engineering*, *56*(10), 7535–7555. https://doi.org/10.1007/s00603-023-03454-5

Zia, H., & Lecampion, B. (2020). PyFrac: A planar 3D hydraulic fracture simulator. *Computer Physics Communications*, *255*, 107368. https://doi.org/10.1016/j.cpc.2020.107368

Zia, H., Perruzo, C., Mori, A., Moukhtari, F.-E., & Lecampion, B. (2024). GeoEnergyLab-EPFL/pyfrac: V1.1.2 [Software]. *Zenodo*. https://doi.org/10.5281/zenodo.10794247